J Comput Neurosci (2007) 22:39–61
DOI 10.1007/s10827-006-9676-3

# On the dynamics of electrically-coupled neurons with inhibitory synapses

**Juan Gao · Philip Holmes**

Received: 30 March 2006 / Revised: 22 June 2006 / Accepted: 5 July 2006 / Published online: 19 September 2006


**Abstract** We study the dynamics and bifurcations of noise-free neurons coupled by gap junctions and inhibitory synapses, using both delayed delta functions and alpha functions to model the latter. We focus on the case of two cells, as in the studies of Chow and Kopell (2000) and Lewis and Rinzel (2003), but also show that stable asynchronous splay states exist for globally coupled networks of $N$ cells dominated by subthreshold electrical coupling. Our results agree with those of Lewis and Rinzel (2003) in the weak coupling range, but our Poincaré map analysis yields more information about global behavior and domains of attraction, and we show that the explicit discontinuous maps derived using delayed delta functions compare well with the continuous history-dependent, implicitly-defined maps derived from alpha functions. We find that increased bias currents, super-threshold electrical coupling and synaptic delays promote synchrony, while sub-threshold electrical coupling and fast synapses promote asynchrony. We compare our analytical results with simulations of an ionic current model of spiking cells, and briefly discuss implications for stimulus response modes of locus coeruleus and for central pattern generators.

**Keywords** Bifurcation diagrams · Electrical coupling · Inhibitory synapses · Integrate-and-fire models · Poincaré maps

**Action Editor: F. Skinner**

J. Gao (✉) · P. Holmes
Department of Mechanical and Aerospace Engineering,
Princeton University, Princeton, NJ 08544, USA
e-mail: jgao@princeton.edu

P. Holmes
Program in Applied and Computational Mathematics,
Princeton University, Princeton, NJ 08544, USA
e-mail: pholmes@math.princeton.edu

## 1 Introduction

Neurons communicate via two basic mechanisms: chemical synapses and electrical gap junctions (Kopell and Ermentrout, 2004; Pfeuty et al., 2003). Synaptic coupling has been well studied, but less work has been done on electrical coupling, although it is widespread in neocortex, hippocampus, cerebellum, and brainstem areas such as locus coeruleus (LC), thalamus, etc. (Merriam et al., 2005; Pfeuty et al., 2003), as well as in central pattern generators such as the lobster stomatogastric ganglion (STG) (Harris-Warrick et al., 1992; Nusbaum and Beenhakker, 2002). The work of Cymbaluk et al. (1994) is an exception, as are recent papers of Kopell and colleagues (Chow and Kopell, 2000; Kopell and Ermentrout, 2004), Lewis and Rinzel (2003) and Chillemi et al. (2005).

Pairs of cells coupled by gap junctions alone are considered in Chow and Kopell (2000) and Lewis (2003), while Chillemi et al. (2005); Kopell and Ermentrout (2004); Lewis and Rinzel (2003); Pfeuty et al. (2005) treat combined electrical and chemical coupling. Various models—integrate and fire (Lewis and Rinzel, 2003), quadratic integrate and fire (Kopell and Ermentrout, 2004), and ionic channel-based (Chillemi et al., 2005)—are used, and analytical methods range from explicit solutions (Chow and Kopell, 2000), through phase reduction and averaging (Lewis and Rinzel, 2003) (which requires weak coupling, cf. Hoppensteadt and Izhikevich (1997)), to numerical simulation (Chillemi et al., 2005). Related work on strong synapses alone, with comparisons to weakly-coupled phase studies, appears in Bressloff and Coombes (2000) and Vreeswijk et al. (1994).

Electrical coupling comprises two parts: a sub-threshold conductive component that draws together membrane voltages of cells in electrical contact, and a super-threshold

component that impulsively increases the voltages of cells in contact with a spiking neuron. As described in Chow and Kopell (2000), Lewis (2003) and Lewis and Rinzel (2003), the former leads to stable asynchronous states, while the latter promotes stable synchrony, so the shapes and "weights" of spikes, and the overall frequency of oscillation (which affects the relative weight of spikes) determine firing patterns. The analysis of strong gap junctions in Chow and Kopell (2000) appears to be the first in which the effects of spike shape are studied systematically. In a different manner, inhibitory synapses can also cause asynchrony or synchrony, depending on synapse time constants (Bressloff and Coombes, 2000; Chow, 1998; Vreeswijk et al., 1994; Wang and Buzskái, 1996). Synchrony is thought to play a role in temporal binding (Merriam et al., 2005; Shadlen and Movshon, 1999; Singer, 1999), and it influences the response of areas such as locus coeruleus involved in neurotransmitter release that in turn affects cortical processes (Alvarez et al., 2002; Aston-Jones and Cohen, 2005; Aston-Jones et al., 1994; Brown et al., 2004; Usher et al., 1999). Spiking and bursting neurons with tunable phase relationships involving both synchrony and antisynchrony are also important in pattern generator circuits (Bem et al., 2005; Bem and Rinzel, 2004; Cymbaluk et al., 1994; Harris-Warrick et al., 1992).

The main goal of this paper is to offer an analytically-tractable integrate-and-fire model for combined electrical and synaptic coupling, and to use it to derive Poincaré maps and bifurcation diagrams for pairs of strongly-coupled cells that allow one to predict the effects of relative coupling strength, spike weight or duty cycle, bias current or intrinsic spiking frequency, and synaptic delays on the existence and stability of synchronous and asynchronous states. We also compare these results with direct simulations of an ionic channel model, and, where appropriate, with works cited above. We are especially indebted to Lewis and Rinzel (2003), in which analogues of many of our results were derived by phase reduction (for weak coupling) and direct construction of periodic solutions (for strong coupling), and to Chow and Kopell (2000), which develops explicit conditions for phase as a function of period, but without computing Poincaré maps per se.

In Section 2, we review and non-dimensionalize the leaky integrate-and-fire (LIF) model, solve for the dynamics between spikes, and derive some basic properties of the spike-to-spike Poincaré map. Section 3 completes our stability and bifurcation analysis for a pair of electrically- and synaptically-coupled cells with simplified, instantaneously-acting "delta function" synapses. In Section 4 we examine the effects of synaptic delays modeled by delayed delta functions and alpha functions, and we show that delays and spike shapes can lead to behaviors not found in the simple delta function models. In Section 5 we simulate a pair of Hodgkin-Huxley (ionic current) spiking neurons and compare their dynamics with predictions of the Poincaré maps derived from integrate-and-fire approximations. Finally, Section 6 summarizes our results and describes implications for the locus coeruleus and CPG circuits.

## 2 The model and a Poincaré map

The dynamics of an LIF neuron is described by an RC circuit:

$$C\frac{dV}{dt} = -g_{\mathrm{L}}(V - V_{\mathrm{L}}) + I_{\mathrm{bias}} + I_{\mathrm{gap}} - I_{\mathrm{syn}}, \tag{1}$$

where $C$ and $g_{\mathrm{L}}$ and $V_{\mathrm{L}}$ denote the membrane capacitance, leakage conductance and resting potential, $I_{\mathrm{bias}}$ is an external bias current, and $I_{\mathrm{gap}}$ and $I_{\mathrm{syn}}$ are electrical and synaptic currents injected from other cells. When $V$ reaches a preset threshold $V_\theta$, a spike is triggered and the voltage reset to $V_{\mathrm{reset}}$. Before further specifying the currents, we remove parameters and nondimensionalize the equations by setting $v = (V - V_{\mathrm{reset}})/(V_\theta - V_{\mathrm{reset}})$ and transforming time by $g_{\mathrm{L}}t/C \mapsto t$. This scales the membrane voltage range to $[0, 1]$, the leak time constant to 1, and rescales the bias, gap junction and synaptic currents as follows:

$$\begin{aligned} \frac{I_{\mathrm{bias}} + g_{\mathrm{L}}(V_{\mathrm{L}} - V_{\mathrm{reset}})}{g_{\mathrm{L}}(V_\theta - V_{\mathrm{reset}})} &\mapsto I_{\mathrm{bias}}, \\ \frac{I_{\mathrm{gap,syn}}}{g_{\mathrm{L}}(V_\theta - V_{\mathrm{reset}})} &\mapsto I_{\mathrm{gap,syn}}. \end{aligned} \tag{2}$$

We model the rescaled gap junction coupling by

$$I_{\mathrm{gap}} = \alpha\left[(v_j - v_i) + \Delta\sum_k \delta\left(t - t_j^k\right)\right], \tag{3}$$

where $j$ denotes a cell making electrical contact with cell $i$ and the sum is taken over the times $t_j^k$ at which the $j$th cell fires (Lewis and Rinzel, 2003). Here $\alpha$ measures the overall electrical coupling strength and $\Delta$ determines the ratio of super-threshold (impulsive) to subthreshold (ohmic) components. In Chow and Kopell (2000) a more detailed spike model is adopted, characterized by three parameters: rise rate, width, and amplitude.

We consider two models for a synapse of strength $\beta$:

$$I_{\mathrm{syn}} = \beta(bv_i - v_{\mathrm{syn}})\sum_k s\left(t - t_j^k\right), \tag{4}$$

where $b = 0$ or 1 and $s(t)$ is a delayed delta function or an "alpha function:"

$$s(t) = \delta(t - t_d) \quad \text{or} \quad \sigma^2 t\exp(-\sigma t), \tag{5}$$

both having unit weight $\int_0^\infty s(t)dt = 1$. Setting $b = 0$ simplifies the analysis and is reasonable when the reversal potential $v_{\rm syn}$ is large and negative, as in strong synapses, and $b = 1$ corresponds to the more usual model which includes the post-synaptic potential (PSP) $v_i$. We use the alpha function with $b = 0$ for direct comparisons with Lewis and Rinzel (2003). Note that, as $\sigma \to \infty$, the alpha function approaches a delta function with $t_d = 0$. Here we only consider inhibitory coupling with negative reversal potential, and we subsequently place reasonable restrictions on coupling strengths $\alpha, \beta \geq 0$, spike weight $\Delta \geq 0$, synaptic delays $t_d \approx 1/\sigma \geq 0$, and $v_{\rm syn} \leq 0$. (For more discussion of synaptic delays and synchrony, see Gerstner et al., 1996).

After rescaling, a pool of $N$ identical, electrically and synaptically-coupled cells may be written as:

$$\frac{dv_i}{dt} = I - v_i + \alpha \sum_{j\neq i} \left[ (v_j - v_i) + \Delta \sum_k \delta\left(t - t_j^k\right) \right] - \beta \sum_{j\neq i} (bv_i - v_{\rm syn}) \sum_k s\left(t - t_j^k\right). \tag{6}$$

We shall assume that the rescaled bias current $I > 1$ so that spiking occurs (at least in the absence of coupling), and as in Chow and Kopell (2000) and Lewis and Rinzel (2003) we shall focus on the case of a pair of identical neurons, although we do include some results on a set of $N$ cells. For arbitrary $N$ it is customary to divide the coupling strengths by $N - 1$ to preserve the same overall strength as $N$ increases: thus $\alpha \mapsto \alpha/(N-1)$, etc.

### 2.1 Preliminary analysis: Two cells with delta spikes

The analysis in this section closely parallels that of Lewis (2003) for a pair of cells without leak ($g_{\rm L} = 0$). We first consider identical cells with instantaneous delta function spikes:

$$\begin{aligned} \frac{dv_1}{dt} &= I - v_1 + \alpha \left[ (v_2 - v_1) + \Delta \sum_k \delta\left(t - t_2^k\right) \right] \\ &\quad -\beta(bv_1 - v_{\rm syn}) \textstyle\sum_k \delta\left(t - t_2^k\right), \\ \frac{dv_2}{dt} &= I - v_2 + \alpha \left[ (v_1 - v_2) + \Delta \sum_k \delta\left(t - t_1^k\right) \right] \\ &\quad -\beta(bv_2 - v_{\rm syn}) \textstyle\sum_k \delta\left(t - t_1^k\right). \end{aligned} \tag{7}$$

In the absence of spiking (or $\Delta = \beta = 0$), and with initial conditions $v_1(0) = \bar{v}_1$, $v_2(0) = \bar{v}_2$, this linear system is easily solved:

$$\begin{aligned} v_1 &= I(1 - e^{-t}) + \left(\frac{\bar{v}_1 + \bar{v}_2}{2}\right) e^{-t} + \left(\frac{\bar{v}_1 - \bar{v}_2}{2}\right) e^{-at}, \\ v_2 &= I(1 - e^{-t}) + \left(\frac{\bar{v}_1 + \bar{v}_2}{2}\right) e^{-t} - \left(\frac{\bar{v}_1 - \bar{v}_2}{2}\right) e^{-at}, \end{aligned} \tag{8}$$

where $a = 1 + 2\alpha$. Hence $v_1 - v_2 = (\bar{v}_1 - \bar{v}_2)e^{-at}$: under the influence of subthreshold coupling (or indeed just leakage alone), the membrane voltages approach one another. However, spikes and resets to zero intervene whenever $v_1$ or $v_2$ reach 1. Assuming that cell 2 has just fired and the system is at $(v_1, v_2) = (\bar{v}_1, 0)$, we compute a Poincaré map from this post-spike state to the next post-spike state immediately after cell 1 fires: indeed, from (8) the interspike interval (ISI) $T = T(\bar{v}_1)$ is determined by:

$$v_1(T) = I(1 - e^{-T}) + \frac{\bar{v}_1}{2}(e^{-T} + e^{-aT}) = 1, \tag{9}$$

and the state of cell 2 when cell 1 fires is:

$$v_2(T) = I(1 - e^{-T}) + \frac{\bar{v}_1}{2}(e^{-T} - e^{-aT}) = 1 - \bar{v}_1 e^{-aT}. \tag{10}$$

Superthreshold electrical coupling adds a further amount $\alpha\Delta$ to $v_2(T)$, and if the synapse is instantaneous ($s(t - t_2^k) = \delta(t - t_2^k)$; $t_d = 0$) synaptic coupling modifies this by additionally subtracting $\beta(bv_2(T) - v_{\rm syn})$. Similar remarks apply in the case that cell 1 fires followed by cell 2. Hence, letting $v$ denote the voltage of the cell that has *not* just fired immediately after the other has fired, we obtain the spike-to-spike Poincaré map and its derivative:

$$v \mapsto f(v) = (1 - \beta b)(1 - ve^{-aT}) + d(\alpha, \beta, b, \Delta, v_{\rm syn}), \tag{11}$$

$$\frac{\partial f(v)}{\partial v} = f'(v) = -(1 - \beta b)e^{-aT}(1 - avT'), \tag{12}$$

where $T = T(v)$ is determined by (9) and we have collected the synaptic and electrical "spike" terms in the parameter $d = (1 - \beta b)\alpha\Delta + \beta v_{\rm syn}$ which superimposes a vertical post-spike jump on $f$, positive if superthreshold electrical coupling dominates synaptic inhibition and negative otherwise. Synaptic delays $t_d > 0$ or the alpha function $s(t) = \sigma^2 t \exp(-\sigma t)$ complicate the situation and we defer a study of these cases to Section 4.

In interpreting the results to follow $v = 1$ and $v = 0$ should be identified, since on spiking $v$ drops instantaneously to 0. Moreover, in common with other models in which intercell communication occurs via delta functions (Hopfield and Herz, 2003), we must decide how to deal with the cases that a positive impulse carries $v$ above threshold ($v = 1$) or a negative impulse takes it below reset ($v = 0$). In the former we assume that a spike occurs immediately: thus, if cell 1 fires when cell 2 is at $v_2(T)$ and $(1 - \beta b)v_2(T) + d \geq 1$, cell 2 fires immediately and thereafter 1 and 2 fire in perfect synchrony: this is the *spike-capture synchrony* of Lewis and Rinzel (2003), also called *absorption* in Mirollo and

Strogatz (1990). In the latter case we allow $v_2$ to drop below 0, so that $v_1$ fires successive spikes and $v_2$'s spikes are suppressed.

The following result, proved in Appendix A, states some general properties of the Poincaré map:

**Proposition 1** *Adopting the convention that if $f(v) \geq 1$ we set $f(v) = 1$, the map $f(v) : [0, 1] \to [0, 1]$ of (11) is continuous except at the endpoints 0 and 1 and possibly at a third point $v_m \in (0, 1)$. $f(v) = 1$ for $v \in [0, v_m]$, $f(1) = 0$, and $f$ is strictly decreasing for $v > v_m$, where $v_m = f^{-1}(1)$ and if $f(v) < 1\ \forall v \in [0, 1]$, $v_m = 0$. Hence $f$ has a fixed point at $v = 0, 1$ and exactly one further fixed point in $(v_m, 1)$, and any other periodic orbit must have period 2.*

Depending upon the size and sign of the post-spike jump $d$ in (11), the value of $v_m$ and the limit $f(1^-)$ the map may take any of the three qualitatively distinct forms shown in Fig. 1. In the first two cases there is a (small) domain $[0, v_m]$ in which $f(v) > 1$ and spike-capture synchrony occurs; we indicate this here and in subsequent Poincaré maps by setting $f(v) \equiv 1$ for $v \in [0, v_m]$. In the first case $[0, v_m]$ is not accessible from the invariant domain $(v_m, 1)$ and all solutions starting in $(v_m, 1)$ limit either on the asynchronous fixed point $v_e$ or on an orbit of period 2, as described further below. In the second, some solutions starting in $(v_m, 1)$ can escape to $[0, v_m]$, resulting in spike capture. These cases are both shown without synaptic coupling ($\beta = 0$), but they can also occur for sufficiently small $\beta$ and $\alpha > 0$. The third case occurs only with $\beta > 0$: here the synchronous state $v = 0$ is completely isolated and a positively-invariant domain surrounds $v_e$, and if $(1 - \beta b)(1 + \alpha\Delta) + \beta v_{\text{syn}} < 0$ (synaptic coupling is sufficiently strong relative to electrical coupling), spike suppression occurs.

All three cases can be regarded as perturbations of the uncoupled system ($\alpha = \beta = 0$), for which $a = 1$, (9) gives $e^{-T} = (I - 1)/(I - v)$ and the map may be written explicitly as

$$f(v) = \frac{I(1 - v)}{I - v}. \tag{13}$$

For this uncoupled system $f(v)$ is smooth and monotonically decreasing on $(0, 1)$ from $f(0^+) = 1$ to $f(1^-) = 0$ and every orbit excepting the neutrally stable asynchronous fixed point

$$v_e = I - \sqrt{I^2 - I}, \quad e^{-T_e} = \sqrt{\frac{I - 1}{I}}. \tag{14}$$

has period 2. In Sections 3 and 4 we will see how specific behaviors emerge by unfolding this degenerate map.

A further elementary result may be noted. If the cells are precisely synchronized ($v_1(t) \equiv v_2(t)$), then after simultaneously spiking both cells climb towards threshold

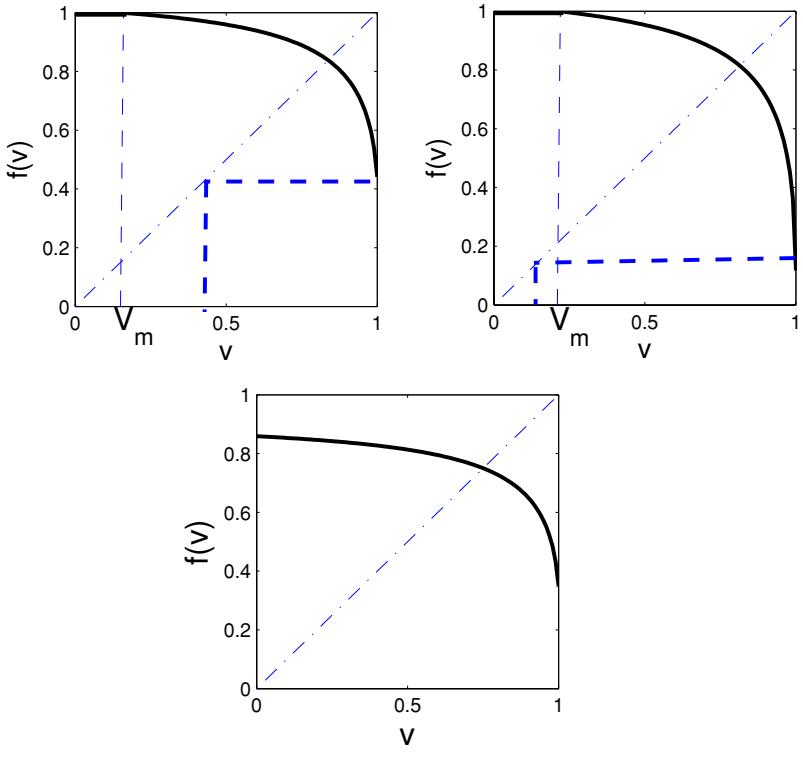


**Fig. 1** Three distinct forms for The Poincaré map $f(v)$ with coexisting synchronous and asynchronous states, showing disjoint domains of attraction ($0 < v_m < f(1^-)$: top left); interleaved domains of attraction ($0 < f(1^-) < v_m$: top right), and an isolated synchronous state ($v_m = 0$: bottom). Parameter values are (a) $I = 1.15$, $\beta = 0$, $\Delta = 0.05$; (b) $I = 1.19$, $\beta = 0$, $\Delta = 0.1$; (c) $I = 1.15$, $\beta = 0.1$, $b = 1$, $\delta = 0.05$; $v_{\text{syn}} = -0.5$ and $\alpha = 0.2$ throughout

$v_j = 1$ from $v_j = d = (1 - \beta b)\alpha\Delta + \beta v_{\text{syn}}$ following the post-spike jump. Integration of (7) yields the ISI for synchronous spiking

$$T_{\text{synch}} = \log\left(\frac{I-d}{I-1}\right), \tag{15}$$

in comparison to the uncoupled ISI $T_e = \log(I/(I-1))$. Note that $T_{\text{synch}} < T_e$ (faster oscillations) for electrical coupling alone, while sufficiently strong instantaneous inhibition, namely

$$\beta > \frac{\alpha\Delta}{\alpha b\Delta - v_{\text{syn}}}, \tag{16}$$

gives $T_{\text{synch}} > T_e$, although as we shall see, only asynchronous solutions are stable in this case. Also, since $d < 1$, it follows from (15) that increases in bias current $I$ with fixed $d$ cause decreases in $T_{\text{synch}}$ and hence increased firing rates. We return to this point in Section 6.

### 2.2 Preliminary analysis: $N$ cells with delta spikes

We may use a similar strategy to solve for interspike behavior in the case of $N$ identical cells with all-to-all electrical coupling (c.f. Bressloff and Coombes (2000) for the synaptic case). Between spikes the system (6) for $1 \le i \le N$ may be written as

$$\dot{\mathbf{v}} = \mathbf{I} + \mathbf{A}\mathbf{v}, \tag{17}$$

where $\mathbf{I} = (I, I, \ldots, I)$ and the $N \times N$ matrix $\mathbf{A}$ may be written

$$\mathbf{A} = \frac{\alpha}{N-1}\begin{bmatrix} 1 & 1 & \ldots & 1 \\ 1 & 1 & \ldots & 1 \\ \vdots & \vdots & \ddots & \vdots \\ 1 & 1 & \ldots & 1 \end{bmatrix} - \left(1 + \frac{N\alpha}{N-1}\right)\begin{bmatrix} 1 & 0 & 0 & \ldots \\ 0 & 1 & 0 & \ldots \\ \vdots & \vdots & \vdots & \ddots \\ 0 & 0 & \ldots & 1 \end{bmatrix}.$$

Here we have made the substitution $\alpha \mapsto \alpha/(N-1)$. A direct computation confirms that $\mathbf{A}$ has eigenvalues $-1$ and $-[1 + N\alpha/(N-1)]$, the latter having multiplicity $N-1$. Transforming to an eigenvector basis via the following matrix of eigenvectors:

$$T = \begin{bmatrix} 1 & 1 & 1 & \vdots & 1 \\ 1 & -1 & 0 & \vdots & 0 \\ 1 & 0 & -1 & \vdots & 0 \\ \vdots & \vdots & 0 & \ddots & \vdots \\ 1 & 0 & \vdots & \vdots & -1 \end{bmatrix},$$

we may solve the system with intial state $v_1(0) = \bar{v}_i$ to obtain:

$$v_i = I(1 - e^{-t}) + \frac{1}{N}\sum_{j=1}^{N}\bar{v}_j e^{-t} + \left(\bar{v}_i - \frac{1}{N}\sum_{j=1}^{N}\bar{v}_j\right)e^{-[1+N\alpha/(N-1)]t}, \tag{18}$$

where $i$ runs from 1 to $N$, thus generalizing the $N = 2$ case of (8).

The analog to the one-dimensional Poincaré map $f$ of (11) is $(N-1)$-dimensional and consequently hard to study, but a "splay-state" solution with equal ISIs $T_e$ and each cell firing with period $NT_e$ can be found rather easily. Setting $b = 0$ for simplicity but allowing post-spike jumps $d = \alpha\Delta + \beta v_{\text{syn}} \neq 0$, we show in Appendix B that there is at least one such solution $T = T_e$ with $y_e = e^{-T_e} \in (0, 1)$. For $d = 0$ and $d$ sufficiently small, we have been able to prove that $T_e$ is unique, but this does not hold for larger $d$, although numerical studies suggest that the solution remains unique and moreover that for $\alpha \neq 0$ and $d$ sufficiently small, this splay state is asymptotically stable. Figure 2 (top panel) shows an example for $N = 3$.

In addition to the splay state there is a synchronous state in which all $N$ cells fire simultaneously ($v_i(t) \equiv v_j(t)$, $\forall i, j$). As for $N = 2$ with $d > 0$ there is a (small) region $v_j > 0$ in which spike-capture synchrony occurs, and so this state is also stable. See Fig. 2 (bottom panel). Chow and Kopell (2000) find splay states and describe parameter ranges in which they exist. Clustered states involving multiple phases have also been found (Golomb and Rinzel, 1994).

## 3 Stability analysis for gap junctions and instantaneous synapses

We now begin our stability and bifurcation analyses, starting with a pair of identical cells with gap junction

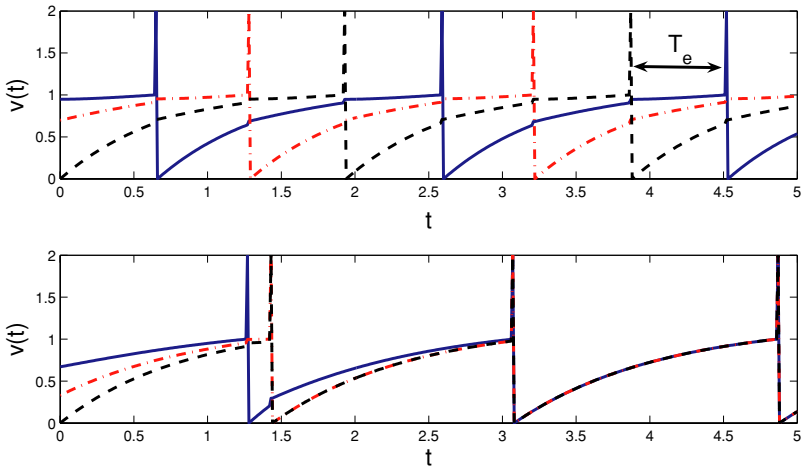


**Fig. 2** A splay state (top) and coexisting synchronous state (bottom) for three coupled cells. Parameter values: $I = 1.2$, $\alpha = 0.2, d = 0.04$ and $b = 0$. Note spike-capture synchrony at second spike in bottom panel

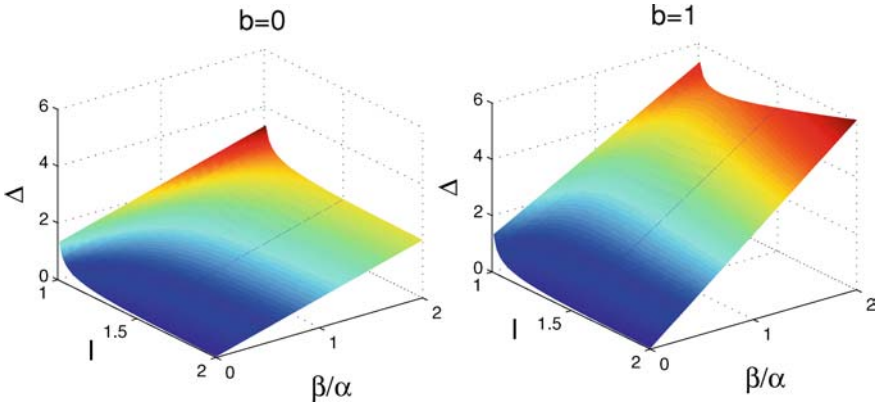


**Fig. 3** Bifurcation sets for the asynchronous state $v_e$ for combined gap junction and instantaneous inhibitory synapses, with ($b = 1$) and without ($b = 0$) the full membrane voltage term in $I_{\text{syn}}$ (Eq. (4)). The full voltage term increases the stability region of $v_e$: below the surfaces

and instantaneous synaptic coupling described by (7). As envisaged in Section 2.1 we perturb from the uncoupled case $\alpha = \beta = 0$. In Section 2.1 we saw that the two quantities $v_m$ and $f(1^-)$ determine the global structure of the map, and from (9) and (11) the asynchronous equilibrium $v_e$ is determined by simultaneous solution of the equations

$$2I(1 - e^{-T}) + v_e(e^{-T} + e^{-aT}) = 2, \quad \text{and} \tag{19}$$

$$v_e = f(v_e) = (1 - \beta b)(1 - v_e e^{-aT_e}) + d, \tag{20}$$

and its local stability by evaluating (12) at $v_e$. Laborious perturbation calculations from the uncoupled equilibrium (14) for *small couplings* $\alpha, \beta$ *of similar order* show that the asynchronous state $v_e$ is stable for

$$\Delta + \overline{\beta} v_{\text{syn}} < s(I, \overline{\beta}) \approx \left(\frac{2I - 1}{2}\right) \log\left(\frac{I}{I - 1}\right) - 1 + \overline{\beta} b I, \tag{21}$$

and unstable for $\Delta + \overline{\beta} v_{\text{syn}} > s(I, \overline{\beta})$, where $\overline{\beta} = \beta/\alpha$ denotes the ratio of synaptic to gap junction strength: details are given in Appendix C. Note that for $\overline{\beta} = 0$ this formula coincides with Lewis and Rinzel (2003, Eq. (11)), which was obtained by an entirely different method using phase response curves and averaging; thus (21) generalizes that result to include synaptic coupling. (note that the teminology differs; in Lewis (2003) and Lewis and Rinzel (2003) $\beta$ plays the role of our $\Delta$). In Fig. 3 we show bifurcation sets in $(I, \Delta, \overline{\beta})$-space for $b = 0$ and $b = 1$. It is interesting to note that setting $b = 1$ (i.e. including the difference $(v - v_{\text{syn}})$ between PSP and reversal potential) increases the domain in which the asynchronous state is stable (the alpha function study of Lewis and Rinzel (2003) sets $b = 0$).

The discussion concerning Fig. 1 towards the end of Section 2.1 shows that the synchronous state is stable for sufficiently large $\alpha$, provided that $v_m > 0$ (spike-capture synchrony). The asynchronous stability condition (21) therefore indicates that bistability can occur in both cases 1 and 2 of Fig. 1. To illustrate this we show a bifurcation diagram and some associated Poincaré maps in Fig. 4. Note that the unstable period 2 orbit and, for low bias current $I$, the discontinuity at $f(1)$, separate the domains of attraction of the synchronous and asynchronous states. Similar maps and bifurcation diagrams for the non-leaky case with gap junction coupling alone appear in Lewis (2003, Figs. 3 and 4), and we note that the branches of unstable orbits derived for strong coupling in Lewis and Rinzel (2003, Figs. 12 and 13), which

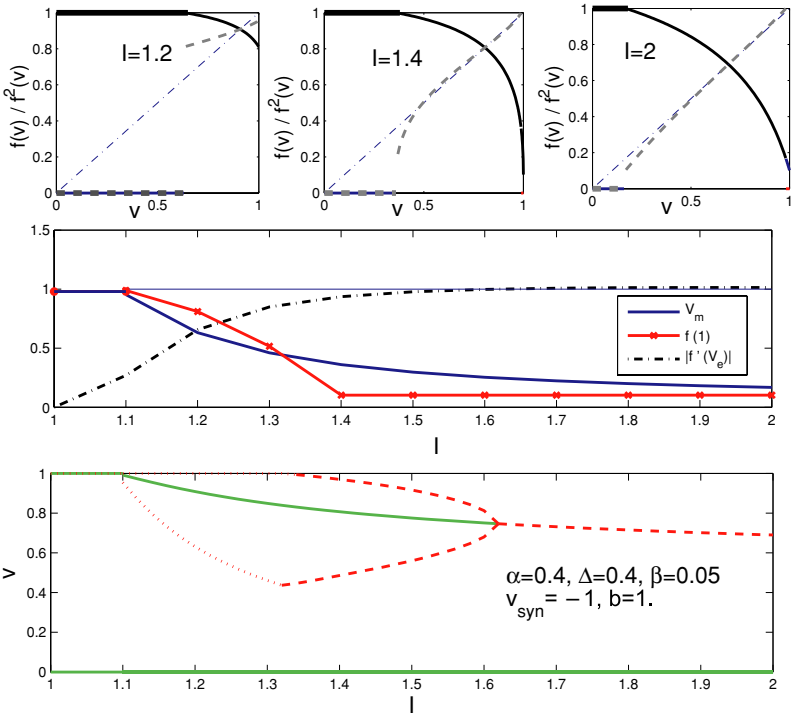


**Fig. 4** Poincaré maps and a bifurcation diagram for a pair of cells with gap junction and instantaneous delta function synapses. The top panels show $f(v)$ (bold) and $f^2(v)$ (dashed) for bias currents $I = 1.2$, 1.4 and 2. The middle panel shows how critical quantities depend on $I$ and the bottom panel shows the asynchronous fixed points $v_e$ and a branch of unstable period 2 orbits arising at the discontinuity in $f$ when $v_m = f(1^-)$ and coalescing with $v_m$ as $I$ decreases. A stable synchronous state ($v = 0, 1$) exists throughout and is globally stable for $1 \le I \le 1.1$. Parameter values: $\alpha = 0.4$, $\Delta = 0.4$, $\beta = 0.05$, $v_{\text{syn}} = -1$, $b = 1$

end before $I = 0$, continue as branches of discontinuities at $f(1)$ in our Poincaré maps.

## 4 Inhibitory synapses with delayed delta and alpha functions

We now consider the influence of synaptic delays, at first using the simple delta function spike model, and then the alpha function of (5), as employed in Lewis and Rinzel (2003). As we shall see, the results are rather complex, and we shall only study the two cell case, and until Section 4.3 we shall consider inhibitory coupling alone ($\alpha = 0$). This significantly simplifies the analysis, since each cell follows its independent uncoupled solution between spikes and jumps:

$$v_i\left(t - t_j^k\right) = I\left(1 - e^{-(t-t_j^k)}\right) + v_i\left(t_j^k\right)e^{-(t-t_j^k)}. \tag{22}$$

It appears easiest to write the map in the form (11) with the argument $v$ replaced by the "virtual" initial condition $\tilde{v}_j$ that would lead, without intermediate jumps, to the post-jump state $v_j(t_i + t_d^+)$. As in Section 2.1 we shall drop the subscripts $i$, $j$ in writing the final expressions for the map, it being understood that $v$ denotes the membrane voltage of the cell that has not just fired.

### 4.1 Inhibition alone: Delayed delta functions

We assume that if cell $i$ fires at time $t_i$, the voltage of cell $j$ drops by $-\beta b v_j + \beta v_{\text{syn}}$ at $t = t_i + t_d$ (recall that $v_{\text{syn}} < 0$ for an inhibitory synapse). Depending on the voltage $v_j(t_i)$ there are several subcases, leading to qualitatively distinct Poincaré maps that can be identified by their firing/jump sequences. We use the notations $f_i$, $d_j$ to denote that $i$ fires and $j$ jumps down respectively.

*Case 0.* $f_i f_j$: Here $v_j$ reaches threshold and fires at $t = t_i + \tau$ before it jumps, with $\tau < t_d$. This is simply the uncoupled case of (13) and it occurs for $v$ close to 1:

$$v \mapsto f_{f_i f_j}(v) = \frac{I(1-v)}{I - v}. \tag{23}$$

*Case 1.* $f_i d_j f_j$: This subsequence occurs when $v_j$ jumps before it reaches 1 and lands above $v_i(t_i + t_d)$. A short calculation using (22) gives the virtual initial condition

$$\tilde{v}_j = (1 - \beta b)v_j(t_i) + \beta v_{\text{syn}} e^{t_d} - \beta b I(e^{t_d} - 1), \tag{24}$$

and ISI

$$e^{-T} = \frac{I - 1}{I - \tilde{v}_j}, \tag{25}$$

so the Poincaré map may be written as

$$\begin{aligned} v \mapsto f_{f_i d_j f_j}(v) &= \frac{I(1-\tilde{v})}{I - \tilde{v}}, \text{ where} \\ \tilde{v} &= (1 - \beta b)v + \beta v_{\text{syn}} e^{t_d} - \beta b I(e^{t_d} - 1). \end{aligned} \tag{26}$$

In the limit $v_j(t_i+t_d) - \beta b v_j + \beta v_{\rm syn} = v_i(t_i + t_d)$, $\tilde{v}_j = 0$, $v_j$ lands exactly on $v_i$ and the two cells fire in synchrony thereafter.

*Case 2.* $f_i d_j f_i$: In this case the jump carries $v_j$ below $v_i$ so that cell $i$ spikes twice in succession. Here the ISI is the time taken for $i$ to climb from 0 to 1: $\exp(-T) = (I-1)/I$ and we have

$$v \mapsto f_{f_i d_j f_i}(v) = 1 + \tilde{v}\left(\frac{I-1}{I}\right), \text{ where} \\ \tilde{v} = (1-\beta b)v + \beta v_{\rm syn} e^{t_d} - \beta b I(e^{t_d}-1). \tag{27}$$

*Case 3.* $f_i d_i d_j f_j$ or $f_i d_i d_j f_i$: This typically follows case 0, here two jumps occur before the next spike and virtual starting points for both cells must be found. The resulting map is:

$$v \mapsto f_{f_i d_i d_j f_j}(v) = \frac{I(1-\tilde{v}_a) + \tilde{v}_b(I-1)}{I - \tilde{v}_a}, \\ \text{if} \quad [I + \beta v_{\rm syn} e^{t_d} - \beta b I(e^{t_d}-1)] \geq 0, \quad \text{and} \tag{28}$$

$$v \mapsto f_{f_i d_i d_j f_j}(v) = \frac{I(1-\tilde{v}_b) + \tilde{v}_a(I-1)}{I - \tilde{v}_b} \quad \text{otherwise}, \tag{29}$$

where

$$\tilde{v}_a = (1-\beta b)v + \beta v_{\rm syn} e^{t_d} - \beta b I(e^{t_d}-1), \tag{30}$$

$$\tilde{v}_b = \beta v_{\rm syn} e^{(t_d-\tau)} - \beta b I\left(e^{(t_d-\tau)}-1\right), e^{-\tau} = \frac{I-v}{I}. \tag{31}$$

Note that the previous interspike interval $\tau$ is related to the initial value $v$ (in the last entry of (31)). In all cases the virtual starting point is a linear function of the post-spike voltage: $\tilde{v} = Av + B$.

Case 3 can degenerate into a further case $f_i d_i f_j$ if the delay $t_d$ is long enough that cell $j$ reaches threshold before it receives synaptic input from cell $i$. This occurs only if $t_d > T_0/2$, where $T_0$ is the ISI for an isolated cell (Eq. (33) below), and we henceforth assume that $t_d < T_0/2$.

The map as a whole is formed by assembling subsets of these maps defined on appropriate domains bounded by two critical values $v_{c0}$ and $v_{c1}$. From $v_{c0}$ the solution $v(t)$ reaches threshold exactly at $t = t_d$:

$$v_{c0}e^{-t_d} + I - Ie^{-t_d} = 1 \Rightarrow v_{c0} = I - (I-1)e^{t_d}. \tag{32}$$

Case 0 ($f_i f_j$) applies for $v \in [v_{c0}, 1)$, and case 1 ($f_i d_i f_j$) applies for $v < v_{c0}$ and sufficiently close to $v_{c0}$. Equation (32) implies that $0 < v_{c0} < 1$ provided $0 < t_d < T_0$, where

$$T_0 = \log\left(\frac{I}{I-1}\right) \tag{33}$$

is the interspike interval for an isolated cell.

The second boundary point $v_{c1}$ separates cases 1 and 2 and is the starting point for a solution $v_j(t)$ that drops exactly onto $v_i(t)$ at $t = t_d$:

$$\tilde{v}_{c1} = (1-\beta b)v_{c1} + \beta v_{\rm syn} e^{t_d} - \beta b I(e^{t_d}-1) = 0; \\ \Rightarrow v_{c1} = \frac{-\beta v_{\rm syn} e^{t_d} + \beta b I(e^{t_d}-1)}{1-\beta b}. \tag{34}$$

Case 1 therefore occurs for $v \in [v_{c1}, v_{c0}]$ and case 2 ($f_i d_j f_i$) occurs for $v \in [0, v_{c1})$. As noted above, case 3 can only follow case 0, and as shown below and in Appendix D, after $v$ falls into $[v_{c0}, 1]$, cases 0 and 3 alternate and the orbit approaches 0 = 1. We do not show the branches $f_{f_i d_i d_j f_j}$ and $f_{f_i d_i d_j f_i}$ in the following figures.

#### 4.1.1 Existence and stability of the synchronous state

We first show that the synchronous state is locally asymptotically stable, although one must correctly interpret the Poincaré map to appreciate this. In particular, for the first two cases of Fig. 5 the values 0 and 1 constitute an orbit of period 2, whose stability is determined by the product of the slopes of the map as $v \to 0$ and $v \to 1$. The relevant branches are $f_{f_i f_j}(v)$ near 1 and $f_{f_i d_i d_j f_j}(v)$ near 0 in the first subcase of case 3, and from (23) and (28) we have:

$$f'_{f_i f_j}(v)\big|_{v=1} = \frac{-I}{I-1}, \\ f'_{f_i d_i d_j f_j}(v)\big|_{v=0} = \frac{-(I-1)[I(1-\beta b) - \beta(k + bIe^{t_d})]}{I[I + \beta k + \beta b I(e^{t_d}-1)]}, \tag{35}$$

where $k = -v_{\rm syn}\exp(t_d) > 0$. In computing the second of these derivatives one must remember that $\tau$ in (31) depends upon $v$. Finally, taking the product of these expressions we obtain:

$$f'_{f_i f_j}(1) f'_{f_i d_i d_j f_j}(0) = \frac{I(1-\beta b) + \beta(v_{\rm syn} - bI)e^{t_d}}{I(1-\beta b) - \beta(v_{\rm syn} - bI)e^{t_d}} \\ \in (-1, 1), \tag{36}$$

so the period 2 orbit is stable, as claimed. In fact for physically-realistic parameters $\beta$, $v_{\rm syn}$ and $t_d$ the derivative lies in (0, 1). A similar calculation using $f_{f_i d_i d_j f_i}$ (31) yields the same conclusion for the second subcase.

Since $v = 1$ implies that the cell will immediately spike and $v = 0$ that it just has spiked, this orbit actually corresponds to a synchronous solution. The analysis shows that as one approaches synchrony, the ISI without jumps decreases towards $\tau = 0$, while the ISI containing the two jumps increases towards

$$T_{\rm synch} = \log\left[\frac{I - \beta v_{\rm syn} e^{t_d} + \beta b I(e^{t_d}-1)}{I-1}\right], \tag{37}$$

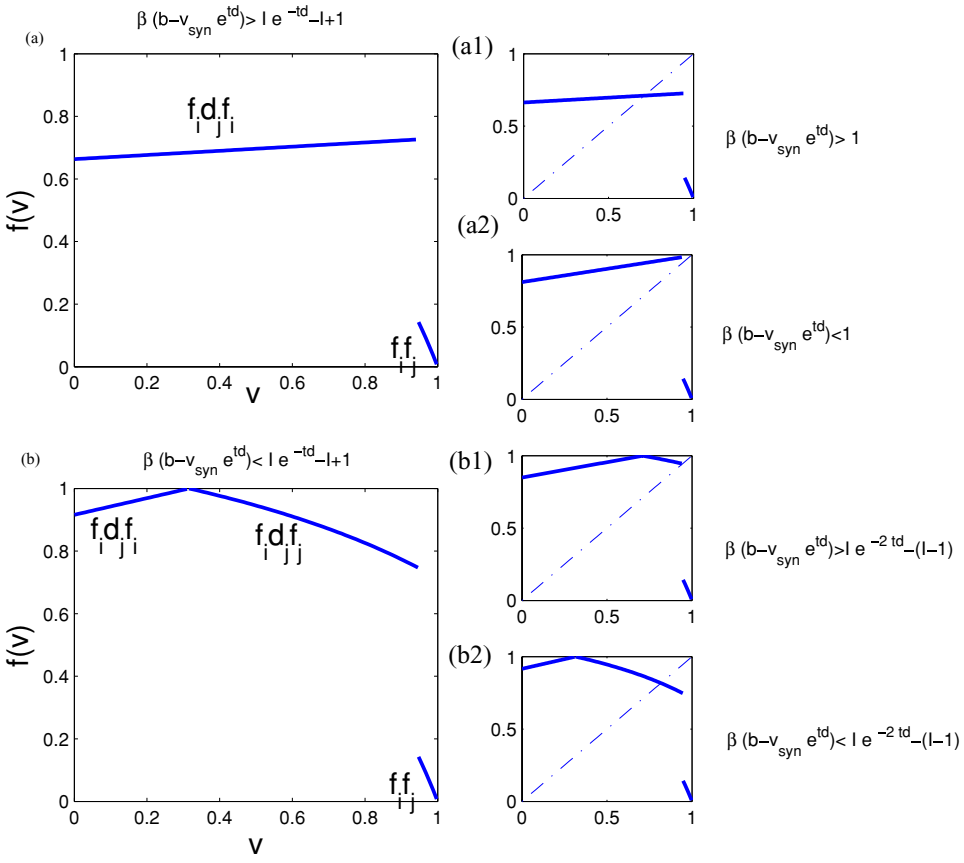


**Fig. 5** Two classes of Poincaré maps for inhibitory synaptic coupling via delayed $\delta$ functions. In the top panels (a) $v_{c1} > v_{c0}$ and cases 0 ($f_{f_i f_j}$) and 2 ($f_{f_i d_j f_i}$) apply; in the lower panels (b) $v_{c1} < v_{c0}$ and cases 0, 1 ($f_{f_i d_j f_j}$) and 2 apply. Each class has two subcases, depending on whether an asynchronous fixed point exists, and spike suppression occurs in case (a1). Parameters are (a) $\beta = 0.8$; (b) $\beta = 0.2$; and (a1) $\beta = 0.8$; (a2) $\beta = 0.45$; (b1) $\beta = 0.36$; (b2) $\beta = 0.2$. $v_{\rm syn} = -1$, $b = 1$, $td = 0.1$ and $I = 1.5$ throughout

as may be seen from (24)–(25). In Appendix D we show that this local stability result may be extended to show that all points in the interval $[v_{c0}, 1]$, and hence all preimages of this interval, converge to the synchronous solution.

Figure 5 shows four qualitatively-distinct maps with branches identified by their firing and jump sequences. These respectively occur when the synaptic coupling strength $\beta(b - v_{\rm syn})$ lies in the intervals $[1, \infty)$, $[Ie^{-t_d} - I + 1, 1)$, $(Ie^{-2t_d} - I + 1, Ie^{-t_d} - I + 1)$ and $[0, Ie^{-2t_d} - I + 1]$, and they fall into two classes, depending upon whether $v_{c1} > v_{c0}$ or $v_{c1} < v_{c0}$. In order of descending coupling strength, we have:

*Form (a1):* There are two branches $f_{f_i d_j f_i}$ and $f_{f_i f_j}$, on the first of which an asynchronous fixed point $v_e$ lies. The conditions $f_{f_i d_j f_i}(v_e) = v_e \le v_{c0}$ and $v_{c1} > v_{c0}$ hold, which, from (27) and (32)–(34) imply that

$$\beta(b - v_{\rm syn}) \ge Ie^{-t_d} - (I - 1) \quad \text{and} \quad \beta(b - v_{\rm syn}) \ge 1 \tag{38}$$

respectively, the latter being the most stringent. Since $f_{f_i d_j f_i}$ is linear in $v$ with slope $0 < (I - 1)(1 - \beta b)/I < 1$, $v_e$ is stable with domain of attraction $(0, v_{c0})$. Hence, for sufficiently large inhibitory coupling

$$\beta\left(b - v_{\rm syn}e^{t_d}\right) > 1 \tag{39}$$

*spike suppression* can occur: one cell fires repeatedly while the other suffers intervening voltage drops that keep it below threshold. As proved above, the synchronous state $0 = 1$ is also stable, so we have bistability. Bressloff and Coombes similarly find spike suppression in large networks (Bressloff and Coombes, 2000, Figs. 6 and 14, called oscillator death) and our criterion (39) agrees qualitatively with theirs, given differences in the PSP models.

*Form (a2):* The branches of (a1) exist, but $f_{f_i d_j f_i}$ does not intersect the diagonal, thus, the first condition of (38) holds but not the second:

$$1 > \beta(b - v_{\rm syn}) \ge Ie^{-t_d} - (I - 1). \tag{40}$$

All points $v \in (0, 1)$ are mapped into $[v_{c0}, 1]$ and eventually to synchrony at $0 = 1$.

*Form (b1):* There are three branches $f_{f_i d_j f_i}$, $f_{f_i d_j f_j}$ and $f_{f_i f_j}$ with no intersection between the second branch and the diagonal. Hence $v_{c1} < v_{c0}$ and $f_{f_i d_j f_j}(v_{c0}) > v_{c0}$, which

together imply:

$$I e^{-t_d} - (I-1) > \beta(b - v_{\text{syn}}) > I e^{-2t_d} - (I-1). \tag{41}$$

As in case (a2) all points are mapped into $[v_{c0}, 1]$ and eventually to 0: no asynchronous state exists.

*Form (b2):* This map shares the first property of (b1) but there is now an asynchronous fixed point $v_e$, so the second property is replaced by $f_{f_i d_j f_j}(v_{c0}) \le v_{c0}$, leading to:

$$I \ge [(I-1) + \beta(b - v_{\text{syn}})]e^{2t_d}. \tag{42}$$

Since $v_e$ lies in the domain of the case 1 map $f_{f_i d_j f_j}$ we may linearise (26) to obtain

$$\left.\frac{\partial f_{f_i d_j f_j}}{\partial v}\right|_{v=v_e} = \left.\frac{-I(I-1)(1-\beta b)}{(I-\tilde{v})^2}\right|_{\tilde{v}=\tilde{v}_e}, \tag{43}$$

and a tedious calculation of the virtual starting point $\tilde{v}_e$ that corresponds to the fixed point $v_e$ shows that (43) lies in $(-1, 0)$, implying stable asynchrony.

As shown above, the synchronous state $0 = 1$ coexists and is also stable, but in this case, unlike (a1), the domains of attraction of the two states may be interlaced. To explore this, we consider the following preimages:

$$u_0 = f^{-1}_{f_i d_j f_j}(v_{c0}) = I + \frac{-\beta v_{\text{syn}} e^{t_d} + \beta b I e^{t_d} - I e^{-t_d}}{1 - \beta b}; \tag{44}$$

$$u_1 = f^{-1}_{f_i d_j f_i}(v_{c0}) = I + \frac{-\beta v_{\text{syn}} e^{t_d} + \beta b I e^{t_d} - I e^{t_d}}{1 - \beta b}. \tag{45}$$

From the strictly positive and negative slopes of the branches $f_{f_i d_j f_i}$ and $f_{f_i d_j f_j}$ and the definitions (32)–(34) of $v_{c1}$ and $v_{c0}$, we deduce that $u_1 < v_{c1} < u_0 < v_{c0}$ (see Fig. 6), and $u_1 < 0$ when $f_{f_i d_j f_i}(0) > v_{c0}$, implying that

$$I(1 - \beta b)(1 - e^{-t_d}) > -\beta v_{\text{syn}} \ (> 0). \tag{46}$$

As proved in Appendix D, all points $v \in [v_{c0}, 1]$ converge to synchrony and all points $v \in (u_0, v_{c0})$ converge to asynchrony. Hence $[u_1, u_0]$ is mapped to $[v_{c0}, 1]$ and thence to synchrony. Similarly, if preimages of $[u_1, u_0]$ and $(u_0, v_{c0})$ exist in $(0, u_1)$, points in them are also mapped to synchrony and asynchrony respectively, and such preimages must alternate, the number of domains being determined by the first pre-image that is less than 0. If (46) holds and $u_1 < 0$, then $(0, u_0]$ is mapped to $[v_{c0}, 1]$ and synchrony. Figure 6 shows an example in which two domains of each type exist.

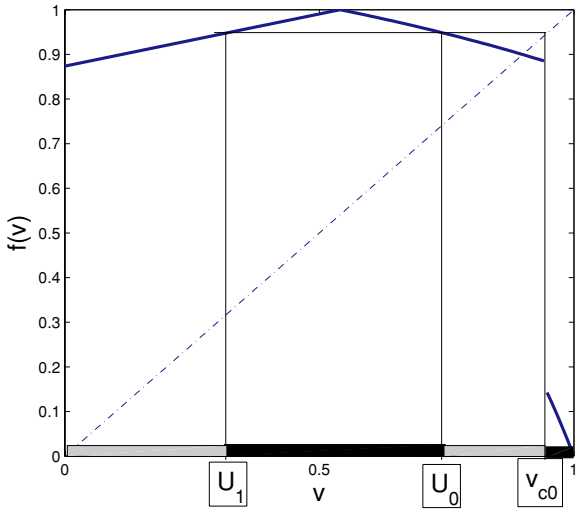


**Fig. 6** Domains of attraction for synchrony (dark) and asynchrony (light) for delayed delta function synapses. Parameters are: $\beta = 0.3$, $v_{\text{syn}} = -1$, $b = 1$, $I = 1.5$, $t_d = 0.1$

### 4.1.2 Bifurcation diagrams

To compare with previous work, we divide the dynamics into three regimes: weak, intermediate, and strong coupling. By weak coupling, we mean that $\beta$ is sufficiently small that (46) holds with $t_d > 0$. As current $I$ or delay $t_d$ increase, the forms (b2) and (b1) appear in sequence; (a1) and (a2) do not occur. For (b1), which occurs for high currents or slow synapses:

$$I \ge I_c \overset{\text{def}}{=} \frac{1 + \beta v_{\text{syn}} - \beta b}{1 - e^{-2t_d}} \quad \text{or}$$
$$t_d \ge \frac{1}{2} \log\left[\frac{I}{I - 1 + \beta(b - v_{\text{syn}})}\right], \tag{47}$$

the entire interval $[0, 1]$ converges to synchrony and there is no asynchronous fixed point. For $I < I_c$ the bistable form (b2) occurs with domains of attraction bounded by $u_0$ and $v_{c0}$. Figure 7 shows bifurcation diagrams in terms of both $I$ and $t_d$; the latter being consistent with Bressloff and Coombes (2000) (Fig. 2(a)), since Bressloff and Coombes' parameter $\alpha \sim 1/t_d$. Figure 8 shows the regions of synchrony and bistability in the $(I, t_d)$-plane, and these are similarly consistent with Lewis and Rinzel (2003, Fig. 5).

Intermediate coupling differs from weak coupling in that (46) is not satisfied and disjoint domains of attraction to synchrony and asynchrony can exist, as in the specific example of Fig. 6, and the form (a2) can also occur, in which all orbits approach synchrony.

For strong coupling (38) always holds; hence form (a1) applies and synchrony and asynchrony coexist unless current $I$ or delay $t_d$ is unreasonably large.

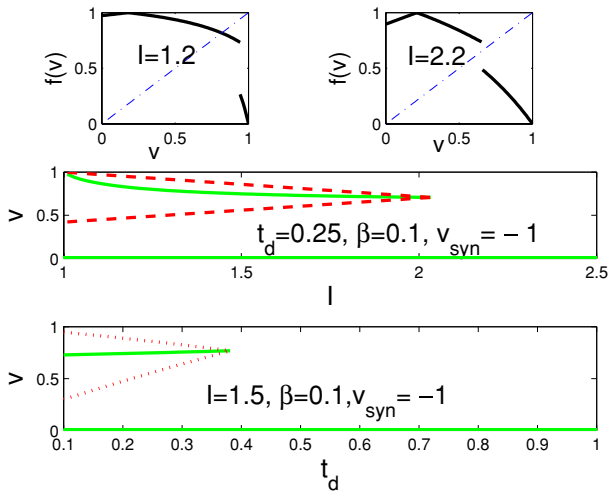


**Fig. 7** Bifurcation diagrams for weak delayed delta function coupling. Top: Poincaré maps for bias currents ($I$) representative of the two regions shown below. Middle and bottom: bifurcation diagrams vs. $I$ and vs. delay $t_d$; asynchronous fixed point vanishes for large $I$ due to discontinuity in map. Parameter values shown on lower panels

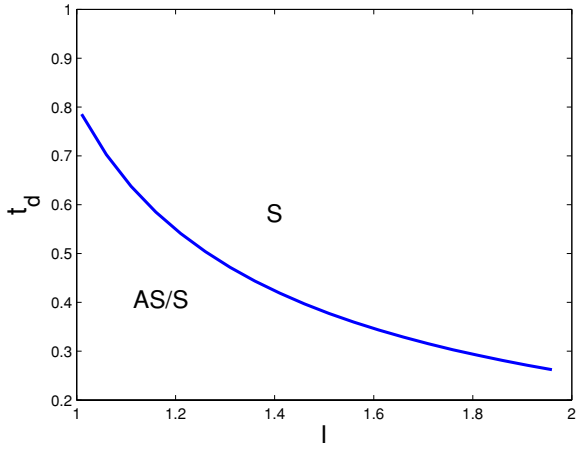


**Fig. 8** A bifurcation set for delayed delta function coupling showing regions in which only synchrony exists (S), and in which synchrony and asynchrony coexist (AS/S)

### 4.2 Inhibition alone: Alpha functions

Turning to the alpha function description of post-synaptic potentials, we face an immediate problem. The decaying exponential (5) persists through many (in principle, all) successive spikes, and so prior history influences the spike-to-spike Poincaré map. If $\sigma$ is relatively large (depending on the ISI), the effects decay rapidly, but we may certainly expect them to persist beyond one ISI, especially for $v \approx 1$, when ISIs are short. Nonetheless, we start by assuming that neuron $i$ has just spiked, and neglect all previous spikes. We only consider the case $b = 0$, as in Lewis and Rinzel (2003). Evolution until the next spike is then determined by:

$$\dot{v}_i = I - v_i, \quad v_i(0) = 0, \tag{48}$$

$$\dot{v}_j = I - v_j + \beta v_{\rm syn}\sigma^2 t e^{-\sigma t}, \quad v_j(0) = v. \tag{49}$$

solutions of which are

$$v_i = I - Ie^{-t}, \text{ and} \tag{50}$$

$$v_j = I - Ie^{-t} + ve^{-t} + \frac{\beta v_{\rm syn}\sigma^2}{(1-\sigma)^2}[(1-\sigma)te^{-\sigma t} - e^{-\sigma t} + e^{-t}]. \tag{51}$$

There are two cases, distinguished by a critical value $v_c$ for which $v_i$ and $v_j$ reach threshold simultaneously at $T = \log[I/(I-1)]$ (from (50)–(51)):

$$v_c = -\frac{\beta v_{\rm syn}\sigma^2}{(1-\sigma)^2}\left[(1-\sigma)\log\left(\frac{I}{I-1}\right)\left(\frac{I}{I-1}\right)^{(1-\sigma)} - \left(\frac{I}{I-1}\right)^{(1-\sigma)} + 1\right]. \tag{52}$$

If $v > v_c$, $v_j(t)$ reaches threshold first, the ISI $T = T(v)$ is implicitly determined by setting $v_j(T) = 1$ and the Poincaré map is

$$v \mapsto f(v) = I - Ie^{-T(v)}. \tag{53}$$

For $v \le v_c$, $v_i(t)$ 'overtakes' $v_j(t)$ and reaches threshold first with ISI $T = \log[I/(I-1)]$ and the Poincaré map is:

$$v \mapsto f(v) = 1 + (v - v_c)\left(\frac{I-1}{I}\right). \tag{54}$$

Figure 9 shows the map derived above, which is continuous and nonsmooth only at at $v = v_c$, along with maps

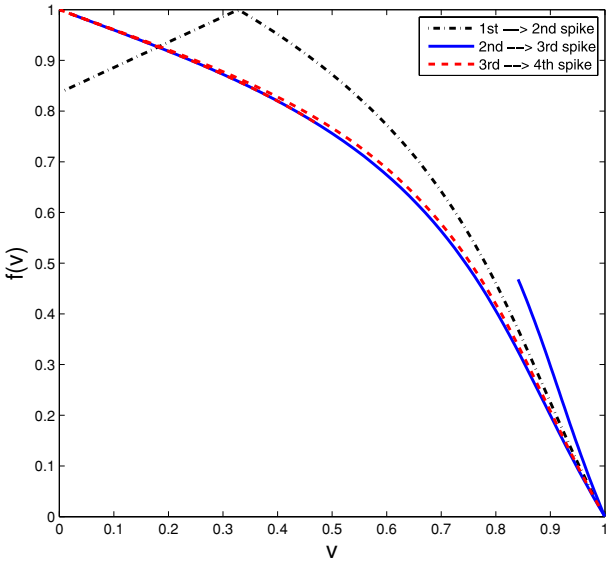


**Fig. 9** Poincaré maps for alpha function coupling neglecting history (black dash-dotted), including one previous spike (blue solid), and two spikes (red dashed). Parameters are $\sigma = 4$, $I = 2$, $\beta = 0.3$

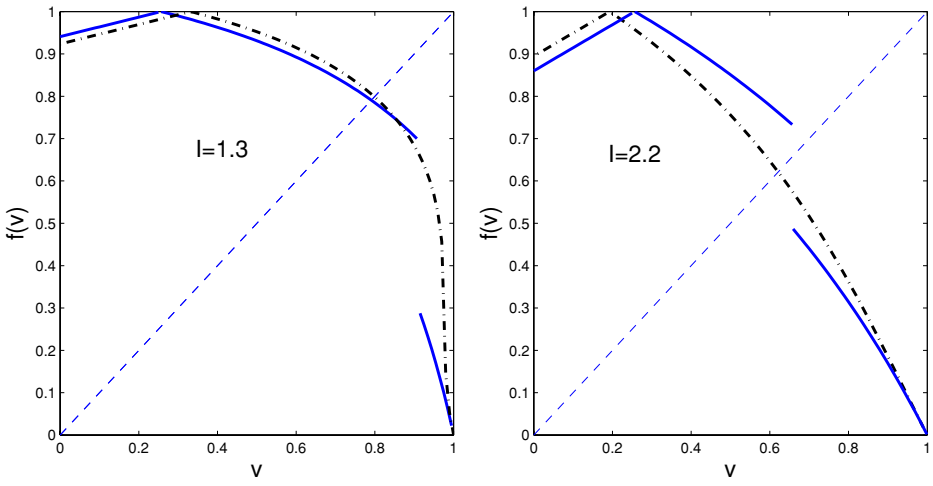


**Fig. 10** Poincaré maps for alpha function coupling (dash-dotted lines) and delayed delta function model (solid lines). Left: $v_{\rm syn} = -1$, $b = 0$, $t_d = 1/\sigma = 0.25$, $I = 1.3$, $\beta = 0.2$: synchrony and asynchrony are both stable. Right: only synchrony is stable; parameters are as at left except that $I = 2.2$

computed numerically by continuing to integrate through three and four spikes respectively, noting the post-spike voltages $v(t_j)$ and $v(t_{j+1})$ and setting $f(v(t_j)) = v(t_{j+1})$ for $j = 2$ and 3. The history-dependence makes the map non-unique for $v$ near 1: the two branches correspond to the histories $f_i f_i$ (upper curve) and $f_j f_i$ (lower curve) respectively, as described in Appendix E. In both cases we can show that solutions started near $v = 0$ or $v = 1$ converge to synchrony, as in the delayed delta function model, although the domain of attraction is slightly smaller in the alpha funtion case (details not given here). Figure 9 shows that as $j$ increases the maps converge. The rate of convergence depends on the synapse time scale $1/\sigma$ and the ISI (determined primarily via $I$).

In Fig. 10 we compare maps derived neglecting history, as above, with those for the corresponding delta model, choosing $t_d = 1/\sigma$ so that the delta function coincides with the peak of the alpha function. The continuity of the alpha funtion map restores the "missing" unstable asynchronous fixed point in the second ($I = 2.2$) case, but we see that otherwise the delta function model provides a reasonable approximation for alpha function coupling. Finally we show an example of a bifurcation diagram in Fig. 11. For this we have used the numerically derived converged map, including history. Qualitative agreement with Fig. 7 is clear (modulo restoration of the unstable asynchronous state past the subcritical period 2 bifurcation), although the bifurcation set for delayed delta function coupling shown in the bottom panel exhibits a larger bias current region in which asynchrony is stable, albeit with smaller domains of attraction. Qualitative agreement holds when $t_d < T_0/2$ and (46) is satisfied. By smoothing the

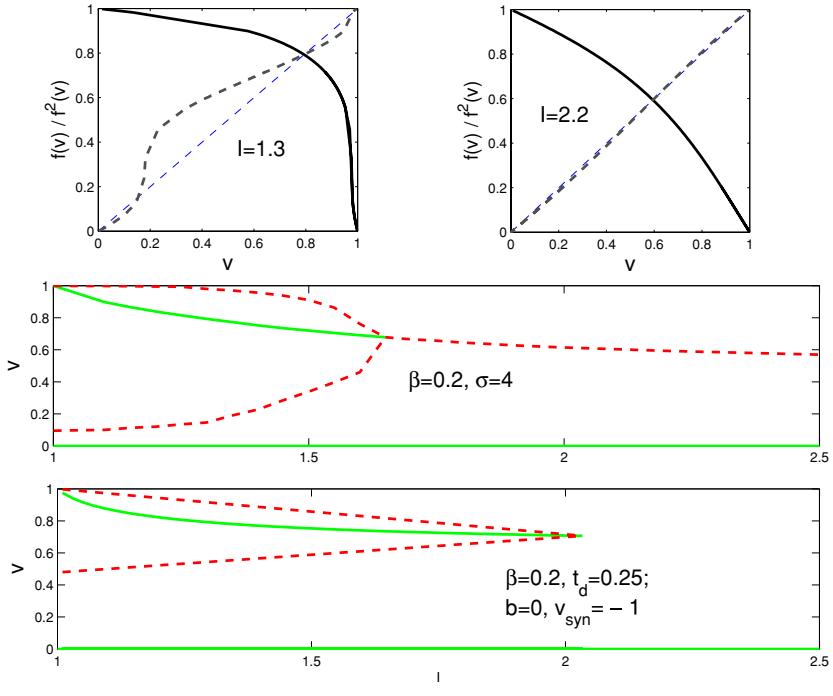


**Fig. 11** Representative Poincaré maps (top, second iterates shown dashed) and bifurcation diagram (middle) for alpha function coupling with $\beta = 0.2$, $\sigma = 4$. Comparable bifurcation diagram for delayed delta function coupling (bottom) for $\beta = 0.2$, $t_d = 1/\sigma = 0.25$, $b = 0$, $v_{\rm syn} = -1$

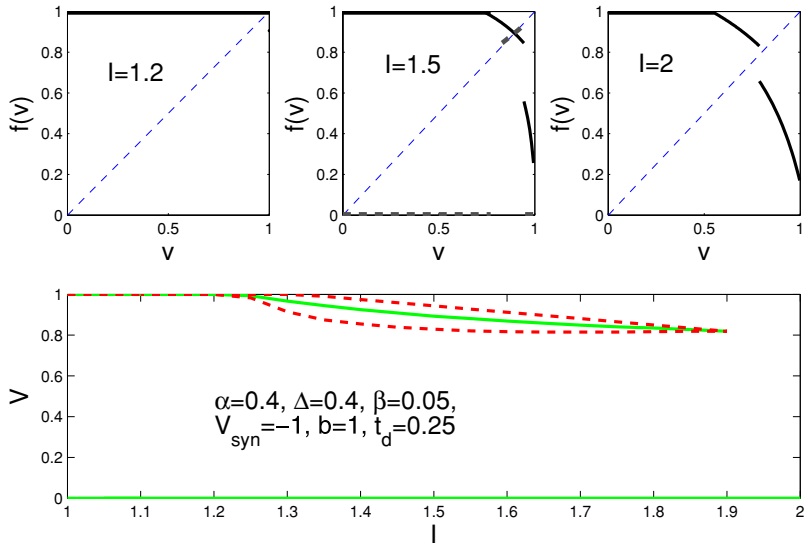


**Fig. 12** Representative Poincaré maps (top) and bifurcation diagram (bottom) for combined electrical and delayed delta function synaptic coupling. For small $I$ only spike-capture synchrony occurs (top left); for intermediate $I$ both synchrony and asynchrony are stable (top middle); for large $I$ only synchrony is stable again (top right). Parameters: $\alpha = 0.4$, $\Delta = 0.4$, $\beta = 0.05$, $v_{\text{syn}} = -1$, $b = 1$, $t_d = 0.25$

internal discontinuity in $f$ due to the delayed delta function, the alpha function produces an unstable asynchronous state much as for electrical coupling (in which the discontinuity occurs at the ends of the domain: $v = 0, 1$).

Van Vreeswijk et al. (1994) and Wang and Buzsáki (1996) have also shown that slow inhibitory synapses lead to synchrony.

### 4.3 Inhibitory and electrical coupling

Having shown in Section 4.2 that the delayed delta function model captures the effects of the alpha function reasonably well, in this section we only consider the combination of gap junction and delayed delta function synapses. The separate effects of electrical and synaptic coupling parameters superposes rather simply. As found in Section 3, increased superthreshold coupling $\Delta$ and bias current $I$ promote synchrony, and as found in Section 4.1 for synaptic coupling the delay $t_d$ and bias current $I$ likewise promote synchrony. When electrical and synaptic coupling work together, it remains true that increases of $\Delta$, $t_d$, or $I$ lead to synchrony.

Figure 12 shows a bifurcation diagram for comparison with that of Fig. 4, from which it differs only in that $t_d = 0.25$ rather than 0. The domain of attraction of synchrony is larger when $t_d > 0$, although the stable asynchronous solution persists for a wider range of bias currents.

## 5 Comparison with an ion-channel model

In this section we report numerical simulations of a Hodgkin-Huxley type ion-channel model of electrically and synaptically coupled neurons. Specifically, we adopt the two-variable reduction due to Rose and Hindmarsh (RH) (1989) of a thalamic neuron model (Connor et al., 1977), with parameters modified to model a pool of LC neurons as in Brown et al. (2004):

$$\begin{aligned} C\dot{V}_i &= \big[I^{\text{RH}}_{\text{bias},i} - g_{Na} m_\infty(V_i)^3(-3(q_i - B b_\infty(V_i)) + 0.85) \\ &\qquad (V_i - V_{Na}) \, , -g_K q_i (V_i - V_K) \\ &\qquad -g_L(V_i - V_L) + I_{\text{ext},i}\big] \\ \dot{q}_i &= (q_\infty(V_i) - q_i)/\tau_q(V_i) \, . \end{aligned} \tag{55}$$

Here $V_i$ is the voltage of neuron $i$, $q_i$ is a collective gating variable, $C$ is cell membrane capacitance, $g_{Na}$, $g_K$, and $g_L$ are maximum conductances for sodium, potassium, and leak currents, and $I^{\text{RH}}_{\text{bias},i}$ is the bias current, which effectively sets ISI. $I_{\text{ext},i}$ denotes extracellular currents due to electrical and synaptic coupling, as described below. The remaining terms $m_\infty(V)$ and $b_\infty(V)$ describe equilibrium levels for fast sodium and potassium channels respectively. Functional forms and parameter values for the RH LC cell model are given in Appendix F.

The external input currents $I_{\text{ext},i}$ are specified as follows:

$$\begin{aligned} I_{\text{ext},i} = I_{\text{gap},i} - I_{\text{syn},i} &= \frac{\alpha^{\text{RH}}}{N-1} \sum_{j \neq i} (V_j - V_i) \\ &\quad - \frac{\beta^{\text{RH}}(V_i - V^{\text{RH}}_{\text{syn}})}{N-1} \sum_{j \neq i} \sum_k A^{\text{RH}}(t - t^k_j), \end{aligned} \tag{56}$$

where the analogue of the alpha function (5) takes the form

$$A^{\text{RH}}(t) = \frac{t}{\tau_A} \exp\left(-\frac{t}{\tau_A}\right), \tag{57}$$

and $V^{\text{RH}}_{\text{syn}}$ is the reversal potential. Note that the signs of the components of $I_{\text{ext},i}$ are chosen to match the convention of Sections 2–4, and differ from those of Brown et al. (2004), Eqs. (1) and (2)), and that we set the delay $t_d = 0$ to agree with the form of (5).

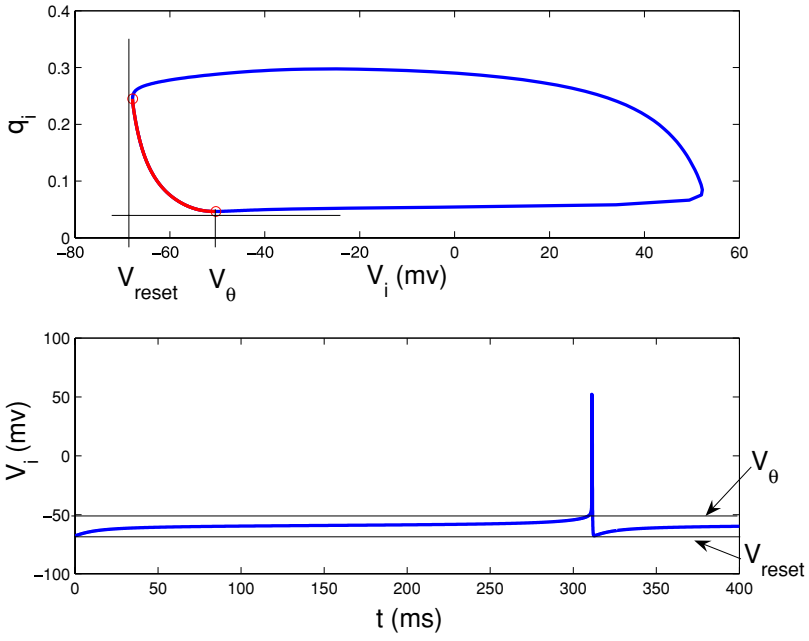


**Fig. 13** The limit cycle of the RH model with LC parameters as specified in Appendix F (top panel) and the time history of the membrane potential (bottom panel), showing how $V_{\text{reset}}$ and $V_\theta$ are defined

To make direct comparisons with the leaky integrate-and-fire (LIF) model (6) considered in Sections 2–4 above, we must map parameters of the ionic current model onto those of the former. We first define reset and threshold voltages for an isolated RH cell by plotting the limit cycle in the $(V_i, q_i)$-phase plane and taking the left and bottom points of vertical and horizontal tangency respectively, as shown in Fig. 13: thus $V_{\text{reset}}$ is defined as the minimum voltage on the limit cycle, and $V_\theta$ is the voltage corresponding to the minimum gating value $q_i$. We use these values in the expression

$$v = \frac{V - V_{\text{reset}}}{V_\theta - V_{\text{reset}}} \tag{58}$$

and those of Eq. (2) that define the rescaled voltage and input currents, although we choose the rescaled bias current $I$ in (6) so that the uncoupled period $T_0 = \log[I/(I-1)]$ matches the nondimensionalised period $g_L T_0^{\text{RH}}/C$ of the RH model. The LIF spike times $t_j^k$ are determined by $V_\theta$, which depends on $I_{\text{bias},i}^{\text{RH}}$. In the following $V_\theta$ varies between $-40$ and $-50$ mV as $I$ varies between 50 and 5 mA; its choice can influence synchrony/asynchrony transitions as noted at the end of this section.

Secondly we determine the super-threshold component of gap junction coupling in the RH system by integrating over the spike:

$$\Delta^{\text{RH}} = \int_{V(t)>V_\theta} (V(t) - V_\theta)dt, \tag{59}$$

and equating the rescaled gap junction currents gives

$$\alpha = \frac{\alpha^{\text{RH}}}{g_L} \quad \text{and} \quad \Delta = \frac{g_L \Delta^{\text{RH}}}{C(V_\theta - V_{\text{reset}})}. \tag{60}$$

For synaptic coupling, using (58) again and equating the rescaled synaptic currents we obtain the equivalences $\sigma = 1/\tau_A$ and

$$\beta = \frac{\tau_A \beta^{\text{RH}}}{C} \quad \text{and} \quad v_{\text{syn}} = \frac{V_{\text{syn}}^{\text{RH}} - V_{\text{reset}}}{V_\theta - V_{\text{reset}}}. \tag{61}$$

We first consider of a pair of identical neurons coupled only via gap junctions ($\alpha > 0, \beta = 0$). Taking the LC model parameter values of Appendix F and integrating forward using a 4–5th order variable step size Runge-Kutta algorithm, we derive a spike-to-spike Poincaré map from the numerical solutions by setting initial conditions of cell 1 at $V_1(0) = V_{\text{reset}}$ and the corresponding value of $q_1(0)$ at the reset point of the unperturbed cycle, taking a range of values $V_2(0) \in (V_{\text{reset}}, V_\theta)$, also with corresponding $q_2(0)$ values, and noting the values $(V_1(t), q_1(t))$ or $(V_2(t), q_2(t))$ directly after the first spike. Doing so, we find that the synchronous solution is stable for *all* bias currents $I_{\text{bias},i}^{\text{RH}}$ greater than $I_{\text{crit}}$, at which isolated cells begin to spike spontaneously via a saddle-node bifurcation on a closed curve (Guckenheimer and Holmes, 1983).

To also obtain stable asynchronous solutions in the RH model we adjusted the spike weight $\Delta_{\text{RH}}$ by changing the time scale $\tau_q(V)$ of the gating variables. Specifically, in place

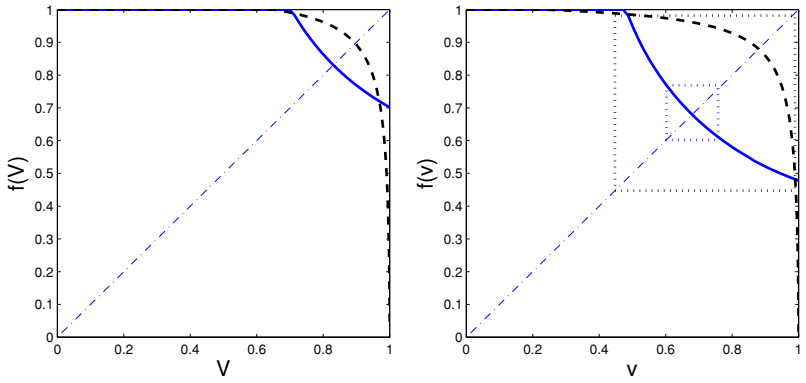


**Fig. 14** Poincaré maps for the RH (solid) and LIF (dashed) models with gap junction coupling $\alpha = 0.025, \beta = 0$. With sufficiently large spike weight $\Delta$ only synchrony is stable (left panel), but with smaller $\Delta$ both synchrony and asynchrony are stable and an unstable period 2 orbit exists (right panel). RH model parameters are $I_{\text{bias}}^{\text{RH}} = 40$ mA, $C_1 = 0.04, C_2 = 5 \Rightarrow f_e' = 1.039$ (left) and $I_{\text{bias}}^{\text{RH}} = 40, C_1 = 0.13, C_2 = 0.05 \Rightarrow f_e' = 0.9879$ (right). LIF parameters are computed as described in text, giving $I = 1.03, \Delta = 1.64 \Rightarrow f_e' = 1.1043$ (left) and $I = 1.03, \Delta = 0.29 \Rightarrow f_e' = 0.8510$ (right)

of the definition given in Appendix F we set the time scales as follows:

$$\tau_q = C_1 \tau_n (\tau_b + C_2), \quad \text{where} \quad \tau_b = \frac{1}{(\alpha_n + \beta_n)^{0.1}} \quad \text{and}$$

$$\tau_n = \frac{3.4 T_b}{1 + e^{V+30}},$$

where $T_b = 1$ msec, and $C_1$ and $C_2$ are constants. This (possibly non-physical) device allows us to conveniently tune the shape of the spike. In Fig. 14 we show RH maps for two parameter choices in comparison with those derived from the LIF model for corresponding parameters (these are both of the type shown in the top left of Fig. 1 and in Fig. 4, including a substantial domain of spike-capture synchrony).

Figure 14 illustrates that while the explicit gap junction coupling maps get the existence and stability types of the synchronous and asynchronous states right, the LIF maps differ significantly in convexity from the RH maps away from the flat spike capture synchrony domain. Comparison of the systems' voltages reveals that this is due to a similar difference in convexity of voltage as a function of time in the latter part of the recovery period: exponential approach to $v = I$ in the LIF case implies that $v$ slows down throughout as it approaches threshold (Fig. 2), while in the RH case, it speeds up as it leaves the neighborhood of the saddle-node bifurcation point between $V_\theta$ and $V_{\text{reset}}$: Fig. 13. This leads to qualitatively different responses to changes in bias current $I$ in the two models, although changes in $\Delta$ have similar effects, as illustrated in Fig. 15: increases in $I$ lower the LIF curve and reduce the spike-capture synchrony domain, while they do the opposite for the RH map; increases in $\Delta$ raise both maps and increase their spike-capture synchrony domains.

The convexity problem might be solved by replacing the classical LIF vectorfield $\dot{v} = I - v + \cdots$ by $\dot{v} = I + v + \cdots$, since the growing exponential reproduces the increase in $\dot{v}$ as the RH voltage approaches threshold. To capture the decrease in $\dot{v}$ following the spike, however, one would need a nonlinear vectorfield, as in the quadratic integrate-and-fire model (Kopell and Ermentrout, 2004), thus precluding simple analysis.

We now turn to inhibitory synaptic coupling ($\alpha = 0, \beta > 0 > V_{\text{syn}}^{\text{RH}}$) and compare the resulting Poincaré map with that of the LIF model with matching alpha function coupling: Fig. 16. Both maps have two branches, that for lower $v$ being almost linear for the RH model, as it is for the LIF system neglecting previous spike history (cf. Fig. 9). As the bias current $I$ increases the branch for larger $v$ moves downward and leftward in both cases, although the convex/concave difference noted above is dramatic: specifically, LIF maps become more convex up and RH maps more concave up with increasing $I_{\text{bias}}$.

In the 4-dimensional phase space of the RH model one cannot easily locate the boundaries of domains of attraction, analogous to the LIF period-2 orbit, so we did not produce bifurcation diagrams to compare with Figs. 11 and 12. However, the RH model also exhibits loss of stability of its asynchronous state and an apparent increase in the domain of attraction of the synchronous state as bias current increases. Specifically, Fig. 17 shows that solutions with out-of-phase initial data remain out of phase for low $I_{\text{bias}}^{\text{RH}} = 10$ mA, while they lock in phase relatively rapidly at higher $I_{\text{bias}}^{\text{RH}} = 40$ mA In comparing RH simulations to the LIF model, the threshold $V_\theta$ plays an important role in timing synaptic release, which in turn determines the bias current at which asynchrony loses stability. For $V_\theta = -30$ in place of the minimum $q_i$ value $-49$ mV, for example, the bifurcation occurs at $I_{\text{bias}}^{\text{RH}} = 15$ mA.

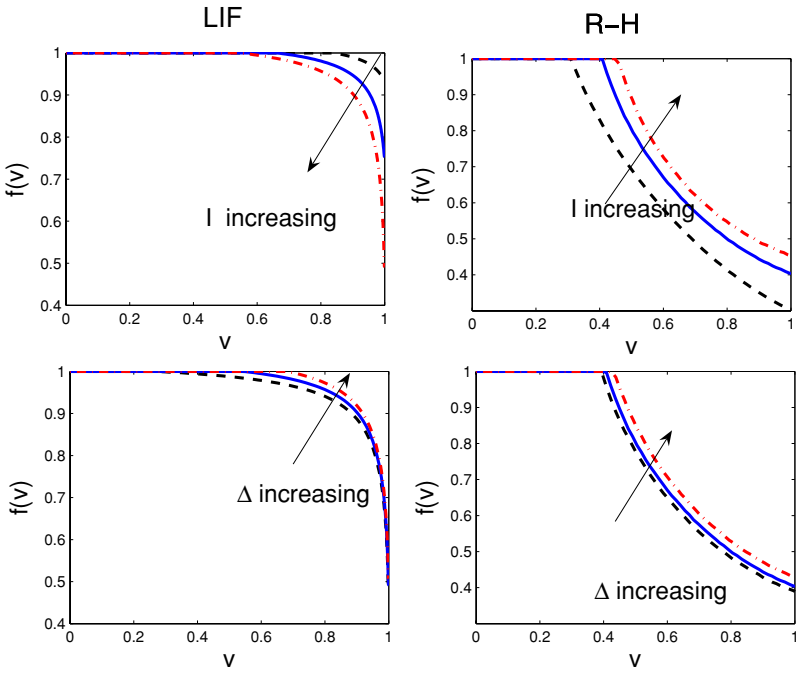


**Fig. 15** Effects of changes in bias current $I$ (top) and spike weight $\Delta$ (bottom) for LIF (left) and RH model (right) with gap junction coupling $\alpha = 0.025$ and $\beta = 0$. In the upper left panel $\Delta = 0.6$ and $I$ increases from 1.01 (dashed) to 1.02 (solid) and 1.03 (dash-dotted); in upper right $I_{\text{bias}}^{\text{RH}} = 20, C_1 = 0.1, C_2 = 0.5$ (dashed), $I_{\text{bias}}^{\text{RH}} = 40, C_1 = 0.1, C_2 = 0.6$ (solid) and $I_{\text{bias}}^{\text{RH}} = 50, C_1 = 0.1, C_2 = 0.6$ (dash-dotted), parameters chosen such that in the corresponding LIF model $\Delta = 0.6$ throughout and $I = 1.0, 1.02, 1.03$ respectively. In the lower left $I = 1.03$ and $\Delta$ increases from 0.2 through 0.4 to 1.0; in lower right $I_{\text{bias}}^{\text{RH}} = 40$ and $(C_1, C_2)$ are (0.108, 0.4), (0.1, 0.6) and (0.09, 1.0), respectively. The corresponding LIF model has $I = 1.02$ and $\Delta = 0.49, 0.64, 0.81$

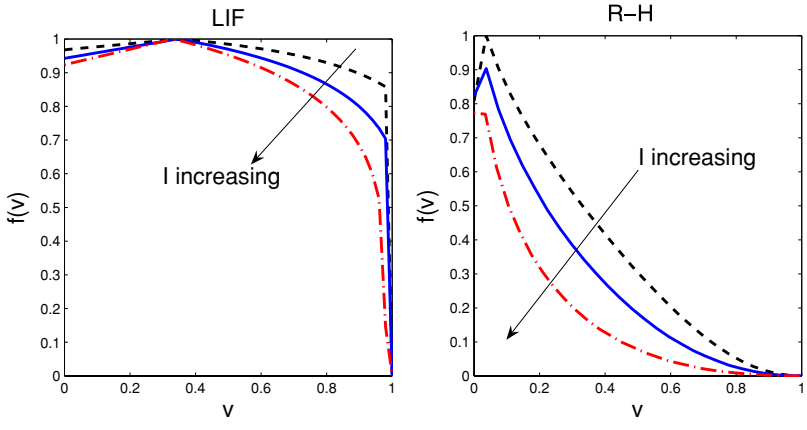


**Fig. 16** Poincaré maps for LIF (left) and RH model (right) with inhibitory synaptic coupling of strength $\beta = 0.2$ and $\alpha = 0$. LIF model has $\sigma = 4$ and $I = 1.1, 1.2, 1.3$ and RH model has $C_1 = 0.04, C_2 = 0.5$, $\tau_A = 0.25$ and $I_{\text{bias}}^{\text{RH}} = 15, 25, 50$ mA

## 6 Conclusion and implications for locus coeruleus and CPG networks

From our LIF analysis with delta function spikes we conclude that, for identical pairs of cells with electrical coupling and inhibitory synapses, three regimes emerge as parameters such as biascurrent $I$ or synaptic to electrical coupling ratio $\beta/\alpha$ vary. For small $I$ spike-capture synchrony is the only stable state; for intermediate $I$ stable synchronous and asynchronous states coexist, their domains of attraction being separated by an unstable period 2 orbit, and for large $I$ synchrony alone is stable, although an unstable asynchronous state continues (except due to artificial discontinuities in the delayed delta function map). See Figs. 3, 4 and 12. We also find that inhibitory synapses can cause spike suppression in which one cell fires while the other oscillates below threshold (Fig. 5(a1)) and the remark preceding Proposition 1).

Synaptic delays and more realistic alpha function spikes modify these results, but overall three factors promote synchrony: (1) strong bias current $I$, which also increases the intrinsic oscillation frequency; (2) large superthreshold electrical coupling or "spike weight" $\Delta$, which promotes spike capture synchrony; and (3) large delays $t_d$ or slow dynamics

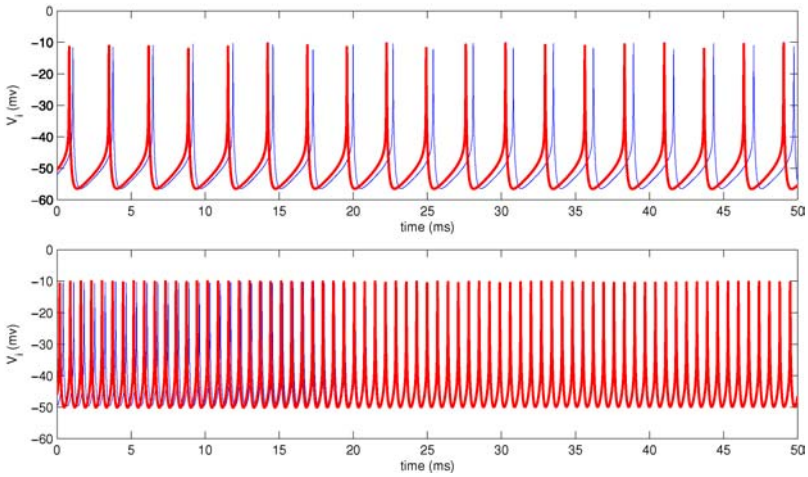


**Fig. 17** Voltage traces for two RH cells (thin blue and thick red) with inhibitory synaptic coupling. Parameters as in Fig. 16 but with $I_{\text{bias}} = 10$ (top) and 40 mA (bottom) respectively

in the inhibitory synapses. In contrast, fast inhibitory synapses and the *subthreshold* component of electrical coupling promote asynchrony, and the latter leads to splay states in multi-unit networks. Our analysis also reproduces the qualitative behavior of the Rose and Hindmarsh (1989) ion-channel based model reasonably well, although the LIF model yields convex Poincaré maps in place of the concave RH maps.

The previous work closest to ours appears to be that of Lewis and Rinzel (2003), as noted in Section 1. Where they are directly comparable, our results agree with theirs, and our global and strongly coupled analysis reveals a period 2 (halting rhythm) separatrix between the synchronous and asynchronous states for moderate bias currents $I$, and shows that a discontinuity in the Poincaré map acts as the separatrix for small $I$. Our analysis also permits direct calculation of oscillation frequencies and conditions for spike-capture synchrony and spike suppression. The results are in general agreement with other studies of combined electrical and chemical coupling (Chillemi et al., 2005; Kopell and Ermentrout, 2004; Pfeuty et al., 2005). The first two of these references explore the effects of heterogeneity and noisy external currents: both important, especially to the cortical applications noted below.

We now briefly indicate implications for two kinds of neural circuitry, and note futher related modeling work.

### 6.1 The locus coeruleus and other brain circuits

The present work was motivated by observations of activity patterns in the brainstem area locus coeruleus (LC) in monkeys performing a target identification task in which they are trained to ignore distractor stimuli. Good performance, defined by low false alarm rates, is associated with relatively slow LC firing in the absence of stimuli, and phasic, correlated responses of LC neurons to targets; faster firing and uncorrelated (tonic) responses accompany poor performance (Aston-Jones et al., 1994). In Usher et al. (1999) this was simulated by modulating the electrical coupling among LC neurons in a hybrid network model in which baseline firing rates were largely determined by additive noise, but no analyses were performed. Subsequently Brown et al. (2004) studied heterogeneous pools of RH neurons reduced to phase oscillators in the limit of weak coupling and low noise, and showed that the target detection results of Aston-Jones et al. (1994) as well as more recent results on a forced choice task (Clayton et al., 2004) could be partially explained in terms of the intrinsic LC frequency set by bias current. The present paper further illuminates these results by addressing the effects of strong coupling, albeit only between identical cells.

Specifically, LC neurons with the parameters of Usher et al. (1999) have a nondimensional spike weight $\Delta \approx 5$ in the LIF reduction: an order of magnitude higher than that used in most of the examples given above. Such a value leads to synchrony even with strong and fast inhibitory coupling, in agreement with phasic response data. Equation (15) is consistent with higher coherent firing rates during stimulus presentation (increases in $I$), but also predicts that increases in electrical coupling $\alpha$ should produce decreased ISIs (provided $(1 - \beta b) > 0$: synaptic coupling is not too strong) and hence *increases* in baseline sychronized firing rates without stimuli, unless inhibitory synapses $\beta$ are also strengthened or bias currents reduced. However, noting that the faster tonic LC state is decorrelated, the pertinent comparison is between asynchronous solutions with low $\alpha$ and synchronous solutions with high $\alpha$, and this depends on other parameters, including noise (Usher et al., 1999), that are absent in our model.

It has also been suggested that slow synaptic inhibition in hippocampal and neocortical circuits can synchronize neurons without the need for gap junctions, thus producing Gamma oscillations. In Wang and Buzsáki (1996) ionic current models with first order ODEs modeling synapses were used to show that synchronization occured best with synaptic time delays around 20% of the uncoupled oscillation period.

### 6.2 Central pattern generators in the stomatogastric ganglion

The stomatogastric ganglion (STG) generates and coordinates motor patterns for foregut movement in crustaceans. It contains approximately 30 neurons, including motoneurons, 11 of which form the central pattern generator (CPG) for the gastric mill and 14 for the pyloric motor network. Pacemaker and passive (driven) neurons can be identified within each sub-network, including endogenous oscillator cells DG and AB in the gastric and pyloric networks respectively, and the half-center oscillator LG/MG/Int1 in the gastric network, which produces an antiphase rhythm (Harris-Warrick et al., 1992).

The STG has become a canonical example of a CPG circuit and its architecture has been largely determined. Most chemical synapses in the gastric network and all in the pyloric network are inhibitory and the electrical connections are non-rectifying, as assumed in our model. It was at first widely accepted that electrical connections synchronize neurons and reciprocal inhibitory synapses desynchronize them, but over the past 20 years it has become clear that details of synaptic coupling can affect this (Marder, 1984; Nusbaum and Beenhakker, 2002). For example, Rowat and Selverston (1997) note that gastric and pyloric synapses are orders of magnitude faster than typical STG oscillation periods, thus yielding asynchrony, while Van Vreeswijk et al. (1994) and Wang and Buzsáki (1996) show that slow inhibitory synapses lead to synchrony, in agreement with the present paper.

In a half-center study Bem and Rinzel (2004) investigated the effects of electrical coupling strength $\alpha$ and duty cycle, which approximately corresponds to our spike weight $\Delta$, in the presence of fast and slow inhibitory synapses, using both relaxation oscillator and ion channel models. They found that the effects of increasing electrical coupling $\alpha$ depend on $\Delta$ in a subtle way: for small duty cycle "almost-in-phase" behavior occurs, followed by antiphase dynamics, coexisting antiphase and synchronous behavior, and ultimately synchrony alone. While some details differ, coexistence of synchrony and asynchrony in a middle range and the facts that increases in $\alpha$ for small $\Delta$ promote asynchrony, while increases in $\Delta$ restabilize asynchrony are echoed by our results. Moreover, our "low $I$" bifurcation initially leads to almost-in-phase behavior as the aynchronous fixed point $v_e$ breaks away from spike-capture synchrony (Figs. 4 and 12). Bem et al. (2005) subsequently performed *in vitro* dynamic clamp experiments on snail neurons to verify the coexistence of synchronous and asynchronous patterns.

Although the LIF model ignores many ionic current and synapse details, our analytical results capture the basic dynamics of electrically and synaptically coupled neurons, providing explicit conditions for synchrony and asynchrony. They contribute to CPG and cortical network theory in predicting that electrical coupling and inhibitory synapses can each promote synchrony or asynchrony depending on spike weight (duty cycle), intrinsic oscillation frequency (bias current), and synapse time scales.

## Appendix A: Proof of proposition 1

The Poincaré map (11) and its derivative (12) depend on the ISI $T(v)$, given implicitly by (9) and we must first distinguish two cases as $v \to 1$, depending on the relative magnitudes of the bias current and subthreshold electrical coupling. If $I \geq (1+a)/2 = 1+\alpha$ then $\dot{v}_1|_{v_1=1,v_2=0} \geq 0$ and $\lim_{v\to 1} T(v) = 0$; if $1 < I < (1+a)/2$ then $\dot{v}_1|_{v_1=1,v_2=0} < 0$ and $\lim_{v\to 1} T(v) = T_1 > 0$, since the subthreshold gap junction coupling dominates the effect of bias current and $v_1$ initially declines immediately after $v_2$ has fired and reset. Figure 18 illustrates this by plotting the functions $l(t) = I(1-e^{-t})$ and $r(t) = 1 - v(e^{-t} + e^{-at})/2$, intersections of which satisfy (9). Clearly $dl/dt - dr/dt = Ie^{-t} - v(e^{-t} + ae^{-at})/2 \geq 0$ for $t \geq 0$ in the first case, by direct calculation and use of $v \leq 1$. In the second case at $v = 1$ $dl/dt - dr/dt < 0$ for $t \in (0, T_c)$, where $ae^{-(a-1)T_c} = 2I - 1$, but since $l'', r'' < 0$, we see that $T_1 > T_c$ and hence $dl/dt \geq dr/dt$ for $t \geq T_1$. This implies that $T(v)$ is strictly decreasing for $v \in (0, 1)$, for from (9) we have

$$T' = -\frac{e^{-T} + e^{-aT}}{2Ie^{-T} - v(e^{-T} + ae^{-aT})}, \tag{62}$$

the denominator of which is $2(dl/dt - dr/dt)$. Since $T' < 0$ and $\beta < 1$ (to keep synaptic depression reasonable), Eq. (12) shows that $f'(v) < 0$ and hence that $f$ decreases as claimed.

The remaining facts that $f(v) = 1$ for $v \in [0, v_m]$ and $v = 1$ follow immediately from the convention chosen to

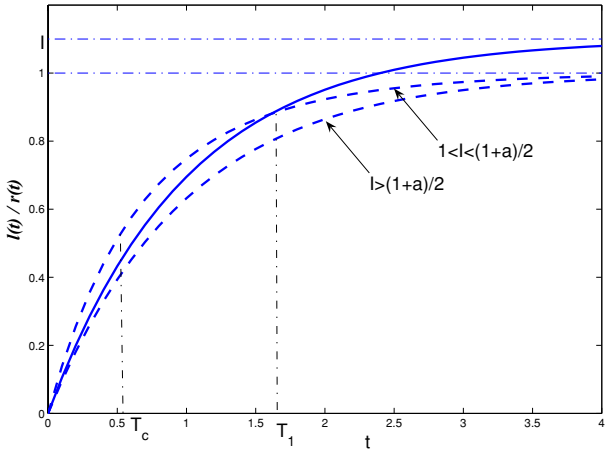


**Fig. 18** The two cases of $\lim_{v\to 1} T(v)$ for $I \geq (1+a)/2$ and $I < (1+a)/2$, with $I = 1.1$. Solid curve shows $l(t)$ and dashed curves show $r(t)$ for $a = 1$ (case 1) and $a = 2$ (case 2)

deal with impulses that take the cell that has not fired over threshold. Since $f'(v) \le 0$, $f$ takes its maximum value at $v = 0$. If $f(0^+) < 1$, then simultaneous spiking cannot occur unless the cells start in perfect synchrony. The discussion regarding $T(v)$ above implies that in case 1

$$\lim_{v\to 1} f(v) = f(1^-) = d, \tag{63}$$

while in case 2:

$$\lim_{v\to 1} f(v) = f(1^-) = (1-\beta b)(1-e^{-T_1}) + d; \tag{64}$$

In either case there may be a discontinuity at $v = 1$.

## Appendix B: Derivation of the $N$-oscillator uniform splay state

Referring to Eq. (18), assuming that cell $N$ has just fired, and denoting the voltages at that instant as $0 = \bar{v}_N < \bar{v}_{N-1} < \cdots < \bar{v}_2 < \bar{v}_1$, we require that $v_j(T) = \bar{v}_{j-1}$ for $2 \le j \le N$ and $v_1(T) = 1$. Using this in (18), adding the post-spike jump $d/(N-1)$ and subtracting the equations pairwise yields:

$$\begin{aligned} 1-\bar{v}_1 &= (\bar{v}_1-\bar{v}_2)e^{-aT} - \frac{d}{N-1}, \ldots\ldots \\ \bar{v}_{j-1}-\bar{v}_j &= (\bar{v}_j-\bar{v}_{j+1})e^{-aT}, \ldots\ldots \\ \bar{v}_{N-2}-\bar{v}_{N-1} &= \bar{v}_{N-1}e^{-aT}, \end{aligned} \tag{65}$$

where $a = [1 + N\alpha/(N-1)]$. Adding the $N$ individual solutions removes the $e^{-aT}$ terms to yield:

$$1 - d = NI(1-e^{-T}) - \bar{V}(1-e^{-T}), \tag{66}$$

where $\bar{V} = \sum_{j=1}^{N-1} \bar{v}_j$. Letting $y = e^{-T}$ and $x = \bar{v}_{N-1}$, and working from bottom to top of (65) we find

$$\begin{aligned} \bar{v}_j &= x\left(1 + y^a + \cdots + y^{(N-j-1)a}\right) \\ &= \frac{x\left(1-y^{(N-j)a}\right)}{1-y^a}, \end{aligned} \tag{67}$$

and

$$1 + \frac{d}{N-1} = \frac{x(1-y^{Na})}{1-y^a}. \tag{68}$$

Finally, substituting (67) into (66), eliminating $x$ via (67) and rearranging yields a single equation for $y$:

$$\begin{aligned} L(y) &\stackrel{\text{def}}{=} N\left(I - \frac{1+d/(N-1)}{1-y^{Na}}\right) \\ &= \frac{1-d}{1-y} - \frac{1+d/(N-1)}{1-y^a} \stackrel{\text{def}}{=} R(y). \end{aligned} \tag{69}$$

Evaluating these expressions we find that $L(0) > R(0)$ and $L(y) - R(y) = -(1-d)/(1-y) + \mathcal{O}(1) < 0$ as $y \to 1$, so there is at least one solution $y_e = e^{-T_e} \in (0,1)$. For $d = 0$ and $d$ sufficiently small, we can show that $\frac{\partial R}{\partial} y - \frac{\partial L}{\partial y} > 0$, implying that $T_e$ is unique, but this fails for larger $d$, although numerical studies suggest that $ye$ remains unique and moreover that for $\alpha \neq 0$ and $d$ sufficiently small, the splay state is asymptotically stable.

From the analysis above we compute the $N$-dimensional generalization of the Poincaré map of (11) componentwise as

$$v_j \mapsto f_j(\mathbf{v}) = 1 + (v_{j+1} - v_1)e^{-aT} + \frac{d}{N-1}, \tag{70}$$

where $\mathbf{v} = (v_1, \ldots, v_{N-1}, 0)$ and $T = T(\mathbf{v})$ is determined by

$$N = NI(1-e^{-T}) + \bar{V}e^{-T} + (Nv_1 - \bar{V})e^{-aT}. \tag{71}$$

The Jacobian derivative is therefore

$$\begin{aligned} \mathbf{Df} = -e^{-aT}\Bigg(&\begin{bmatrix} 1 & -1 & 0 & \ldots \\ 1 & 0 & -1 & 0 \\ \vdots & \ddots & \vdots & \\ 1 & 0 & \ldots & -1 \end{bmatrix} \\ &-a\begin{bmatrix} v_1 - v_2 \\ v_1 - v_3 \\ \vdots \\ v_1 - 0 \end{bmatrix}\begin{bmatrix} \frac{\partial T}{\partial v_1}, & \frac{\partial T}{\partial v_2}, & \ldots, & \frac{\partial T}{\partial v_{N-1}} \end{bmatrix}\Bigg), \end{aligned} \tag{72}$$

which may be evaluated at $\bar{v}_j$ and $T_e$ in terms of $x$ and $y$ to yield stability information.

## Appendix C: Perturbation calculation for gap junction and delta synapse model

We perturb from the asynchronous uncoupled state with fixed point given by (14):

$$v_0 = I - \sqrt{I^2 - I}, \quad e^{-T_0} = \sqrt{\frac{I-1}{I}}, \tag{73}$$

by assuming $\alpha$ and $\beta$ of the same (small) order and letting $\overline{\beta} = \frac{\beta}{\alpha}$ denote the ratio of synaptic to electrical coupling. Specifically, we substitute

$$v_e = v_0 + \alpha v_1 + \mathcal{O}(\alpha^2), \quad T_e = T_0 + \alpha T_1 + \mathcal{O}(\alpha^2) \tag{74}$$

into (19)–(20), noting that $d = \alpha(\Delta + \overline{\beta} v_{\rm syn}) + \mathcal{O}(\alpha^2)$, and equate terms of $\mathcal{O}(\alpha)$ to obtain:

$$I T_1 + v_1 - T_1 v_0 - T_0 v_0 = 0 \quad \text{and} \tag{75}$$

$$e^{-T_0}(2T_0 v_0 + T_1 v_0 - v_1) - v_0 \overline{\beta} b + \Delta + \overline{\beta} v_{\rm syn} - v_1 = 0. \tag{76}$$

For convenience, we set $\widetilde{\Delta} = \Delta + \overline{\beta} v_{\rm syn}$ for the rest of this calculation. Solving (75)–(76) gives the first order corrections:

$$v_1 = \frac{T_0 + \widetilde{\Delta} - v_0 \overline{\beta} b}{2}, \quad T_1 = \frac{T_0(2v_0 - 1) + v_0 \overline{\beta} - \widetilde{\Delta}}{2\sqrt{I^2 - I}}. \tag{77}$$

To compute the derivative $f'(v_e)$ we substitute $T'$ from (62) into (12) and use the ISI condition (19) to obtain a general expression valid for any $v \in (v_m, 1)$:

$$f'(v) = -(1 - \alpha \overline{\beta} b)\left[\frac{e^{-(1+a)T}(I + \alpha v)}{a(I-1) - \alpha(2I - v)e^{-T}}\right]. \tag{78}$$

Noting that $d = \alpha \widetilde{\Delta} + \mathcal{O}(\alpha^2)$, the equilibrium conditions (19)–(20) can be rewritten as:

$$e^{-aT_e} = \frac{1 - \overline{\beta} b \alpha - v_e + \alpha \widetilde{\Delta}}{(1 - \overline{\beta} b \alpha) v_e} + \mathcal{O}(\alpha^2), \quad \text{and} \tag{79}$$

$$e^{-T_e} = \frac{(2I-2)(1 - \overline{\beta} b \alpha) + 1 - v_e + \alpha(\widetilde{\Delta} - \overline{\beta} b)}{(1 - \overline{\beta} b \alpha)(2I - v_e)} + \mathcal{O}(\alpha^2). \tag{80}$$

Substituting (79)–(80) into (78) and using (73) and (74), after some effort we obtain

$$f'(v_e) = -\left[\frac{I(I-1) + \alpha \mathbb{A}}{I(I-1) + \alpha \mathbb{B}}\right] + \mathcal{O}(\alpha^2), \tag{81}$$

where

$$\mathbb{A} = (I - v_0)[2I\widetilde{\Delta} + 1 - v_0 - 2I v_1] - 2I \overline{\beta} b (2I - I v_0 - 1), \tag{82}$$

$$\mathbb{B} = (I - v_0)[-v_0 + 2(I-1)v_1] - I \overline{\beta} b (I - 1). \tag{83}$$

In deriving these expressions we repeatedly use the equalities $v_0^2 - 2I v_0 + I = 0$ and $(1 - v_0)(2I - 1 - v_0)I = v_0(I-1)(2I - v_0) = I(I-1)$, which are satisfied by the unperturbed solution (73). We observe that for $\alpha = 0$, $f'(v_0) = -1$, and $v_0$ is neutrally stable, as noted at the end of Section 2.1.

Since $f'(v) < 0$ (Proposition 1), we require $f'(v_e) \in (-1, 0)$ for stability. Clearly $I(I-1) + \mathcal{O}(\alpha) > 0$ for $\alpha$ sufficiently small, so it suffices to check that $\mathbb{A} < \mathbb{B}$. This finally yields the condition:

$$\widetilde{\Delta} < (2I - 1)T_0 - 1 + \overline{\beta} b I. \tag{84}$$

Recalling that $\widetilde{\Delta} = \Delta + \overline{\beta} v_{\rm syn}$ and $T_0 = \log \sqrt{I/(I-1)}$ we obtain (21).

## Appendix D: Domains of attraction for delayed-delta synapse model

*The synchronous state*

We show in Section 4.1 that the synchronous state is locally asymptotically stable. Here we additionally prove that the interval $[v_{c0}, 1]$ is positively invariant and that all points in it converge to synchrony. We first consider the composition of cases 0 and the first subcase of 3:

$$F(v) = f_{f_i d_i d_j f_j} \cdot f_{f_i f_j}(v) \quad \text{for} \quad v \in [v_{c0}, 1]. \tag{85}$$

We shall show that $F$ is an increasing function satisfying $F(v) > v$ and $F'(v)_{v=1} < 1$ which together imply that $\{F^j(v)\}_0^\infty$ is an increasing series with upper limit 1.

We recall the expressions

$$f_{f_i f_j}(v) = \frac{I(1-v)}{I - v}, \quad f'_{f_i f_j}(v) = -\frac{I(I-1)}{(I-v)^2},$$

and to make the analogous expressions for $f_{f_i d_i d_j f_j}$ and $F$ more compact, we define $\Omega = -\beta v_{\rm syn}$, $K = \Omega e^{t_d}$, $A = \beta b I e^{t_d}$, $B = \beta b I$, thereby obtaining:

$$f_{f_i d_i d_j f_j}(v) = 1 - \frac{(I-1)(I - A - B - K)v}{I[I + K + A - B - (1 - \beta b)v]},$$

$$F(v) = 1 - \frac{(I-1)(I-A-B-K)(1-v)}{[I(I+A+K-B) - (I-B) - (K+A)v]};$$

$$f'_{f_i d_i d_j f_j}(v) = -\frac{(I-1)(I-A-B-K)(I+K+A-B)}{I[I+K+A-B-(1-\beta b)v]^2},$$

$$F'(v) = \frac{(I-1)^2(I-A-B-K)(I+A+K-B)}{[I(I+A+K-B) - (I-B) - (K+A)v]^2}.$$

We note that $I + K + A - B > 0$ and $I + K + A - B - (1 - \beta b)v > 0$ for $v \in [0, 1]$. Since $f_{f_i d_i d_j f_j}(v) < 1$, it follows that $[I - A - B - K] > 0$ and hence that $f'_{f_i d_i d_j f_j}(v) < 0$ and $F'(v) > 0$ (the latter also follows from the fact that $f'_{f_i f_j}(v) < 0$). Figure 19 shows the two branches of the map and the second iterate.

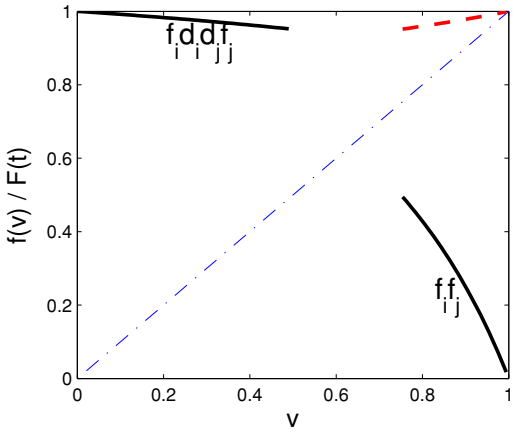


**Fig. 19** The maps $f_{f_i d_i d_j f_j}$ and $f_{f_i f_j}$ and their composition $F$ (dashed). Parameters: $\beta = 0.2$; $I = 1.5$; $v_{\text{syn}} = -1$; $t_d = 0.4$; $b = 1$

Now $f_{f_i d_i d_j f_j}$ is a decreasing function with range $[f_{f_i d_i d_j f_j}(v_{c2}), 1]$, where $v_{c2} = f_{f_i f_j}(v_{c0}) = I(1 - e^{-t_d})$ (from (23) and (32)), and so the range of $f_{f_i d_i d_j f_j}$ lies within the domain $[v_{c0}, 1]$ of $f_{f_i f_j}$ provided that $f_{f_i d_i d_j f_j}(v_{c2}) \geq v_{c0}$. We compute

$$f_{f_i d_i d_j f_j}(v_{c2}) = I - (I-1)\frac{[(K+A)e^{-t_d} + (I-B)]}{[(K+A) + (I-B)e^{-t_d}]}, \tag{86}$$

and since the inequality

$$\frac{(K+A)e^{-t_d} + (I-B)}{(K+A) + (I-B)e^{-t_d}} \leq e^{t_d} \Leftrightarrow (K+A)e^{-t_d} \leq (K+A)e^{t_d}$$

holds for all $t_d \geq 0$, we see that $f_{f_i d_i d_j f_j}(v_{c2}) \geq v_{c0}$ is indeed satisfied. Moreover, this implies that $F(v_{c0}) > v_{c0}$, and hence that $F(v) > v$; $\forall v \in [v_{c0}, 1]$.

In the event that cases 0 and the second subcase of 3 alternate, we have $[I - A - B - K] < 0$ and a similar argument using $f_{f_i d_i d_j f_i}$ yields the same conclusion.

*The asynchronous state*

We now verify that for maps of the form (b2) all points $v \in (u_0, v_{c0})$ converge to asynchrony by showing that this interval is positively invariant and that the second iterate $F = f^2_{f_i d_j f_j}$ of the appropriate map has slope less than 1. Using the same definitions of $\Omega$, $K$, $A$, $B$ as above, we compute

$$f_{f_i d_j f_j}(v) = I - \frac{I(I-1)}{[I + K + A - B - (1-\beta b)v]},$$

$$F(v) = I - \frac{I(I-1)[I + K + A - B - (1-\beta b)v]}{\{(I-1)(I-B) + (K+A)[I + K + A - B - (1-\beta b)v]\}},$$

with derivatives:

$$f'_{f_i d_j f_j}(v) = -\frac{(I-1)(I-B)}{[I + K + A - B - (1-\beta b)v]^2} < 0,$$

$$F'(v) = \frac{[(I-1)(I-B)]^2}{D^2},$$

where $D$ denotes the denominator of the final term of $F(v)$. It is clear that $F'(v) > 0$. Moreover, since by assumption $I(1 - \beta b) = I - B > 0$, $K + A > 0$ and $I + K + A - B - (1 - \beta b)v > 0$, it follows that $F'(v) \in (0, 1)$.

Invariance follows from the fact that inequality (42) holds for (b2) (i.e. $[I - 1 + \Omega + \beta b]e^{2t_d} \leq I$), which in turn implies

$$f_{f_i d_j f_j}(v_{c0}) = I - \frac{I(I-1)}{[I - 1 + \Omega + \beta b]e^{t_d}} \geq u_0$$
$$= I + \frac{(\Omega + \beta b)e^{t_d} - Ie^{-t_d}}{1 - \beta b}, \tag{87}$$

and hence that $f_{f_i d_j f_j}(u_0, v_{c0}) \subset (u_0, v_{c0})$.

## Appendix E: Alpha functions with two interspike intervals history

Suppose that neuron $i$ has just fired and that the previous spike came from neuron $j$ with an ISI of $\bar{T}$. Then the next phase is described by

$$\dot{v}_i = I - v_i - \beta\sigma^2(t + \bar{T})e^{-\sigma(t+\bar{T})}, \quad v(0) = 0,$$
$$\dot{v}_j = I - v_j - \beta\sigma^2 te^{-\sigma t}, \quad v(0) = v,$$

the solutions of which are:

$$v_i(t) = I - Ie^{-t} - p_i(t) \quad \text{and}$$
$$v_j(t) = I - Ie^{-t} + ve^{-t} - p_j(t),$$

where

$$p_i = \frac{\beta\sigma^2 e^{-\sigma\bar{T}}}{1-\sigma}[te^{-\sigma t} + \bar{T}e^{-\sigma t} - \bar{T}e^{-t}] + \frac{\beta\sigma^2 e^{-\sigma\bar{T}}}{(1-\sigma)^2}[e^{-t} - e^{-\sigma t}],$$

$$p_j = \frac{\beta\sigma^2}{(1-\sigma)^2}[(1-\sigma)te^{-\sigma t} - e^{-\sigma t} + e^{-t}].$$

On the other hand, if neuron $i$ fires two spike in a row, we have:

$$\dot{v}_i = I - v_i, \quad v(0) = 0,$$
$$\dot{v}_j = I - v_j - \beta\sigma^2 te^{-\sigma t} - \beta\sigma^2(t + \bar{T})e^{-\sigma(t+\bar{T})}, \quad v(0) = v,$$

with solutions

$$v_i(t) = I - Ie^{-t} \quad \text{and}$$
$$v_j(t) = I - Ie^{-t} + ve^{-t} - p_j(t) - p_i(t).$$

In neither case can we find explicit expressions for the Poincaré map or analogues of $v_c$, but it may be computed numerically by continuing the solutions of Section 4.2 for one further ISI using the expressions above. The two distinct one-previous-spike histories ($f_jf_i$ and $f_if_i$) are responsible for the two branches of the map of Fig. 9.

## Appendix F: Parameter values for the Rose-Hindmarsh equations

Parameter values and function definitions of the Rose-Hindmarsh model (55) are as follows:

$$V_{Na} = 55 \text{ mV}, V_K = V_{\text{syn}} = -72 \text{ mV}, v_L = -17 \text{ mV},$$
$$g_{Na} = 120 \text{ mS/cm}^2, g_K = 20 \text{ mS/cm}^2,$$
$$g_L = 0.3 \text{ mS/cm}^2,$$
$$g_A = 47.7 \text{ mS/cm}^2, C = 1 \ \mu\text{F/cm}^2,$$
$$I_{\text{bias},i} = 5 \ \mu\text{A/cm}^2, \gamma_b = 0.069 \text{ mV}^{-1},$$
$$T_b = 1 \text{ msec}, T_n = 0.52 \text{ msec}, B = 0.21 g_A/g_K,$$
$$q_\infty(v) = n_\infty(v)^4 + Bb_\infty(v),$$
$$b_\infty(v) = (1/(1 + \exp(\gamma_b(v + 53.3))))^4,$$
$$m_\infty(v) = \alpha_m(v)/(\alpha_m(v) + \beta_m(v)),$$
$$n_\infty(v) = \alpha_n(v)/(\alpha_n(v) + \beta_n(v)),$$
$$\tau_q(v) = (\tau_b(v) + \tau_n(v))/2, \ \ \tau_n(v) = T_n/(\alpha_n(v) + \beta_n(v)),$$
$$\tau_b(v) = T_b(1.24 + 2.678/(1 + \exp((v + 50)/16.027))),$$
$$\alpha_n(v) = 0.01(v + 45.7)/(1 - \exp(-(v + 45.7)/10)),$$
$$\alpha_m(v) = 0.1(v + 29.7)/(1 - \exp(-(v + 29.7)/10)),$$
$$\beta_n(v) = 0.125 \exp(-(v + 55.7)/80),$$
$$\beta_m(v) = 4 \exp(-(v + 54.7)/18).$$

**Acknowledgments** This work was supported by DoE grant DE-FG02-95ER25238 and PHS grants MH58480 and MH62196 (Cognitive and Neural Mechanisms of Conflict and Control, Silvio M. Conte Center). We thank the reviewers for their comments and for drawing our attention to relevant work of which we were unaware.

## References

Alvarez VA, Chow CC, Van Bockstaele EJ, Williams JT (2002) Frequency-dependent synchrony in locus coeruleus: role of electrotonic coupling. Proc. Natl. Acad. Sci. 99(6): 4032–4036.

Aston-Jones G, Cohen, JD (2005) An integrative theory of locus coeruleus norepinephrine function: adaptive gain and optimal performance. Ann. Rev. Neurosci. 28: 403–450.

Aston-Jones G, Rajkowski J, Kubiak P, Alexinsky T (1994) Locus coeruleus neurons in the monkey are selectively activated by attended stimuli in a vigilance task. J. Neurosci. 14: 4467–4480.

Bem T, Le Feuvre Y, Rinzel J, Meyrand P (2005) Electrical coupling induces bistability of rhythms in networks of inhibitory spiking neurones. Preprint, Laboratoire de Neurobiologe des Réseaux, Université de Bordeaux.

Bem T, Rinzel J (2004) Short duty cycle destabilizes a half-center oscillator, but gap junctions can restabilize the antiphase pattern. J. Neurophysiol. 91: 693–703.

Bressloff PC, Coombes S (2000) Dynamics of strongly coupled spiking neurons. Neural. Comp. 12: 91–129.

Brown E, Moehlis J, Holmes P, Clayton E, Rajkowski J, Aston-Jones G (2004) The influence of spike rate and stimulus duration on brainstem noradrenergic neurons. J. Comp. Neurosci. 17(1): 13–9.

Chillemi S, Panarese A, Barbi M, Di Garbo A (2005) Gap-junctions promote synchrony in a network of inhibitory interneurons in the presence of heterogeneities and noise. In: Mira J, Alvarez JR, eds. IWINAC 2005, Lecture Notes in Computer Science. Springer-Verlag, pp. 77–85.

Chow C (1998) Phase locking in weakly heterogeneous neuronal networks. Physica D 118: 343–370.

Chow CC, Kopell N (2000) Dynamics of spiking neurons with electrical coupling. Neural. Comp. 12: 1643–1678.

Clayton E, Rajkowski J, Cohen JD, Aston-Jones G (2004) Phasic activation of monkey locus coeruleus neurons by simple decisions in a forced choice task. J. Neurosci. 24: 99124–9920.

Connor J, Walter D, McKown R (1977) Neural repetitive firing: modifications of the Hodgkin-Huxley axon suggested by experimental results from crustacean axons. Biophys. J. 18: 81–102.

Cymbaluk GS, Nikolaev EV, Borisyuk RM (1994) In-phase and antiphase oscillations in a model of two electrically-coupled pacemakers. Biol. Cyb. 71: 153–160.

Gerstner W, van Hemmen JL, Cowan JD (1996) What matters in neuronal locking. Neural. Comp. 94: 1653–1676.

Golomb D, Rinzel J (1994) Clustering in globally-coupled inhibitory neurons. Physica D 72: 259–282.

Guckenheimer J, Holmes P (1983) Nonlinear oscillations, dynamical systems, and bifurcations of vector fields. Springer-Verlag.

Harris-Warrick RM, Marder E, Selverston AI, Moulins M (eds.) (1992) Dynamic biological networks: the stomatogastric nervous system. MIT Press.

Hopfield JJ, Herz AVM (2003) Rapid local synchronizaiton of action potentials: toward computaion with coupled integrate-and-fire neurons. Proc. Natl. Acad. USA 92: 6655–6662.

Hoppensteadt FC, Izhikevich E (1997) Weakly connected neural networks. Springer-Verlag.

Kopell N, Ermentrout GB (2004) Chemical and electrical synapses perform complementary roles in the synchronization of interneuronal networks. Proc. Nat. Acad. Sci. 101(43): 15482–15487.

Lewis TJ (2003) Phase locking in electrically-coupled non-leaky integrate-and-fire neurons. Discrete and Continuous Dynamical Systems, Supplementary volume, Proc. 4th Int. Conf. on Dynamical Systems and Differential Equations. pp. 554–562.

Lewis TJ, Rinzel J (2003) Dynamics of spiking neurons connected by both inhibitory and electrical coupling. J. Comp. Neurosci. 14: 283–309.

Marder E (1984) Roles for electrical coupling in neural circuits as revealed by selective neuronal detections. J. Exp. Biol. 112: 147–167.

Merriam EB, Nethoff TI, Banks MI (2005) Bistable network behavior of layer I interneurons in auditory cortex. J. Neurosci. 25(2): 6175–6186.

Mirollo RE, Strogatz SH (1990) Synchronization of pulse-coupled biological oscillators. SIAM J. Appl. Math. 50: 1645–1662.

Nusbaum MP, Beenhakker MP (2002) A small-systems approach to motor pattern generation. Nature 417: 343–350.

Pfeuty B, Mato G, Golomb D, Hansel D (2003) Electrical synapses and synchrony: the role of intrinsic currents. J. Neurosci. 23: 6280–6294.

Pfeuty B, Mato G, Golomb D, Hansel D (2005) The combined effects of inhibitory and electrical synapses on synchrony. Neural. Comp. 17: 633–670.

Rose R, Hindmarsh J (1989) The assembly of ionic currents in a thalamic neuron I. The three-dimensional model. Proc. R. Soc. Lond. B 237: 267–288.

Rowat PF, Selverston AI (1997) Oscillatory mechanisms in pairs of neurons connected with fast inhibitory synapses. J. Comp. Neurosci. 4: 103–127.

Shadlen MN, Movshon JA (1999) Synchrony unbound: a critical evaluation of the temporal binding hypothesis. Neuron. 24: 67–77.

Singer W (1999) Neuronal synchrony: a versatile code for the definition of relations. J. Comp. Neurosci. 24: 49–65.

Usher M, Cohen JD, Servan-Schreiber D, Rajkowsky J, Aston-Jones G (1999) The role of locus coeruleus in the regulation of cognitive performance. Science 283: 549–554.

Van Vreeswijk C, Abbott LF, Ermentrout GB (1994) When inhibition not excitation synchronizes neural firing. J. Comp. Neurosci. 1: 313–321.

Wang XJ, Buzsáki G (1996) Gamma oscillation by synaptic inhibition in a hippocampal interneuronal network model. J. Neurosci. 16: 6402–6413.